catalysts

MDPI

Review

Recent Advances in Photocatalytic CO_2 Utilisation Over Multifunctional Metal–Organic Frameworks

Priyanka Verma, Daniel J. Stewart and Robert Raja *

School of Chemistry, University of Southampton, Highfield, University Road, Southampton SO17 1BJ, UK; P.Verma@soton.ac.uk (P.V.); Daniel.Stewart@soton.ac.uk (D.J.S.)

* Correspondence: R.Raja@soton.ac.uk

Received: 14 September 2020; Accepted: 7 October 2020; Published: 13 October 2020

Abstract: The efficient conversion of carbon dioxide (CO_2) to high-value chemicals using renewable solar energy is a highly attractive but very challenging process that is used to address ever-growing energy demands and environmental issues. In recent years, metal–organic frameworks (MOFs) have received significant research attention owing to their tuneability in terms of their composition, structure, and multifunctional characteristics. The functionalisation of MOFs by metal nanoparticles (NPs) is a promising approach used to enhance their light absorption and photocatalytic activity. The efficient charge separation and strong CO_2 binding affinity of hybrid MOF-based photocatalysts facilitate the CO_2 conversion process. This review summarises the latest advancements involving noble metal, non-noble-metal, and miscellaneous species functionalised MOF-based hybrid photocatalysts for the reduction of CO_2 to carbon monoxide (CO) and other value-added chemicals. The novel synthetic strategies and their corresponding structure–property relationships have also been discussed for solar-to-chemical energy conversion. Furthermore, the current challenges and prospects in practical applications are also highlighted for sustainable energy production.

Keywords: metal–organic frameworks; photocatalysis; CO_2 utilisation

1. Introduction

The continuous increase in the greenhouse gas (CO_2) concentration in the atmosphere has become a global environmental concern [1,2]. To mitigate this environmental issue, significant research efforts have been directed towards CO_2 capture and storage (CCS) to decrease the level of emissions [3–5]. However, the high costs involved in CO_2 capture and transportation restrict the practical application of this process. Direct CO_2 conversion into value-added chemicals such as CO, methanol, and other hydrocarbons [6] is a promising route to overcome the dependency on non-renewable fossil fuels [7–9]. However, a significant amount of energy is required to break the highly stable molecules of CO_2, which have a bond enthalpy of 805 kJ mol^{-1}. Therefore, the use of abundant and reliable solar energy to carry out the photocatlytic CO_2 reduction is appealing and has received tremendous research attention for the sustainable conversion of solar energy to chemical energy by mimicking the natural photosynthetic process [10–16]. The CO_2 photoreduction product formation is dependent on the number of electrons and protons transferred in the reaction, as summarised in Equations (1)–(7) in Table 1, along with their reduction potentials compared to normal hydrogen electrodes (NHE) at pH 7.0 [17]. The photocatalytic CO_2 reduction process involves three main steps: (i) visible light absorption by the photocatalyst, (ii) generation of charge carriers, and (iii) efficient adsorption and activation of CO_2 on the surface of photocatalyst [18]. In the past few decades, research efforts have been focused on expanding the visible light absorption by incorporating the multifunctional properties of photocatalysts to promote the conversion efficiency [19–25]. However, the current development concerning the photocatalytic efficiency for CO_2 reduction is far from satisfactory because of the fast recombination of charge carriers,

lower specific surface area values, and poor CO_2 adsorption capacity of photocatalysts. Therefore, it is important to design and develop photocatalysts that can address the aforementioned issues. CO_2 reduction using photothermal and thermochemical conversions, where enhanced yields using localised high temperatures generated via thermal relaxation processes have been reported [26–31], are mainly facilitated by surface reactions. However, in this review, we focus exclusively on photocatalytic reduction of CO_2, with a primary focus on metal–organic frameworks.

Table 1. Multielectron reactions of CO_2 reduction and their reduction potentials at pH 7.0 with reference to a normal hydrogen electrode (NHE) at 25 °C and 1 atm.

Equation Number	Reaction	Reduction Potential (V) vs. NHE
1	$CO_2 + 2H^+ + 2e^- \rightarrow HCOOH$	−0.61
2	$CO_2 + 4H^+ + 4e^- \rightarrow HCHO + H_2O$	−0.53
3	$CO_2 + 2H^+ + 2e^- \rightarrow CO + H_2O$	−0.48
4	$CO_2 + 6H^+ + 6e^- \rightarrow CH_3OH + H_2O$	−0.38
5	$CO_2 + 8H^+ + 8e^- \rightarrow CH_4 + 2H_2O$	−0.24
6	$H_2O \rightarrow \frac{1}{2} O_2 + 2H^+ + 2e^-$	+0.82
7	$2H^+ + 2e^- \rightarrow H_2$	−0.41

Metal–organic frameworks (MOFs) are a new class of porous solids prepared by linking multi-dentate organic ligands with a metal or metal clusters, leading to the development of single-site solid catalysts [32–36]. They have emerged as promising materials for a range of applications, including acid-based catalysis [37–40], redox reactions [41–43], drug delivery [44–48], asymmetric reactions [49–55], gas sorption [56–59], and photocatalysis [60–64], because of their large surface areas and high levels of porosity. In particular, MOFs are promising for photocatalysis due to the flexible ways in which they can be tailored toward a specific property. A number of structural parameters, such as the pore size, shape, topology, dimensionality, and chemical environment, can be altered through careful selection of the metal clusters and organic linkers that constitute their building blocks [65]. The structural arrangement assists in the integration of active sites and photosensitisers in a single material through metal nodes and organic linkers, allowing the development of multifunctional MOFs. Their hierarchical organisation allows the incorporation of both light absorption and catalytic components to achieve efficient solar utilisation in artificial photosynthesis. MOF-5 was amongst the first photoactive MOF materials studied for its charge separation efficiency under light irradiation, which led to the further development of various semiconducting MOFs for photocatalytic applications [66,67]. The functionalisation of MOFs can be carried out in situ or by post-synthetic modification (PSM). In situ functionalisation can be achieved using various ligands or metals during the synthesis of MOFs, while the post-synthetic approach involves the modification of the synthesised parent MOF by introducing organic functionalities, metal nanoparticles (NPs), oxides, carbon heterostructures, amines, and quantum dots [68].

MOFs are promising materials for photocatalytic CO_2 reduction for the following reasons: (i) their light absorption properties can be tuned, leading to improved charge separation efficiency; (ii) they possess the capability to capture CO_2; (iii) the constituent metal and organic linkers can participate in the catalytic reaction; (iv) the structural porosity allows access of guest molecules to active sites for efficient photocatalytic reduction [69,70]. Figure 1a illustrates the process of photocatalytic CO_2 reduction over MOFs under solar light irradiation. Although there are several published review papers summarising the synthesis, strategies, and applications in photocatalytic reactions, it is essential to provide a timely progress of the recent research advances in this field [17,18,71–82]. Figure 1b displays the continuous increase in the thousands of publications reported every year based on MOFs and CO_2 reduction reactions, showing the popularity of this field amongst scientists around the world. In this comprehensive review article, we present the recent advancements on the synthesis and catalytic application of functionalised MOFs. The article is divided into three different sections focusing on the visible light responsive MOFs functionalised by (i) noble metal NPs, (ii) non-noble metal NPs, and (iii)

miscellaneous species for photocatalytic CO_2 reduction to CO, methane (CH_4), methanol (CH_3OH), and other value-added chemicals. The factors affecting the efficiency of CO_2 reduction, including the lifetimes of charge carriers and the CO_2 adsorption ability, are also reviewed. Finally, the current challenges and future opportunities of MOFs for photocatalytic CO_2 reduction are discussed.

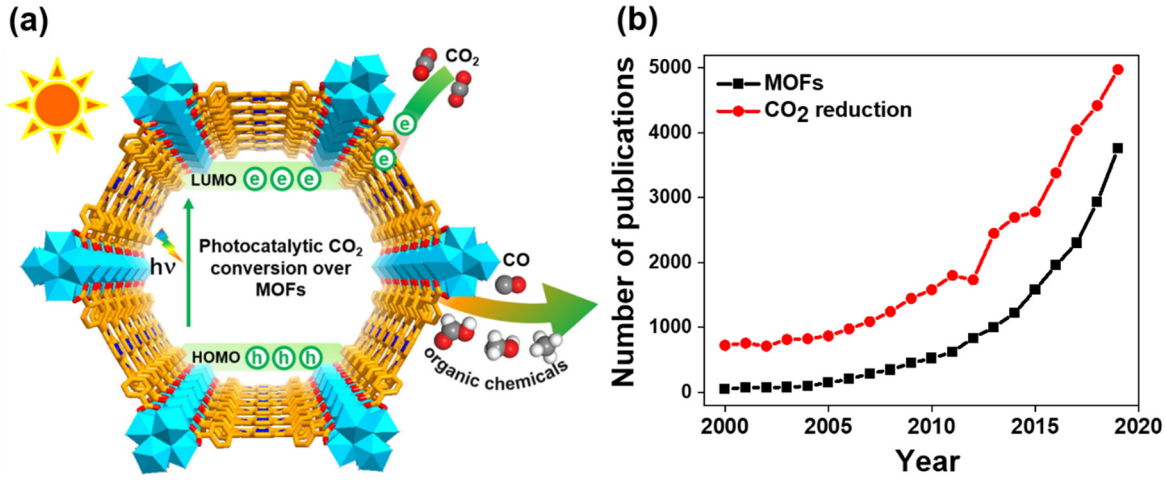

Figure 1. (**a**) Schematic illustration depicting photocatalytic CO_2 reduction into CO and value-added chemicals over metal–organic frameworks (MOFs). (**b**) Number of publications in the last 20 years along with the averages calculated from Scopus, Web of Science, and SciFinder for the entries "MOFs" and "CO_2 reduction" as of September 2020. Figure 1a reproduced with permission from [81]. Copyright 2020, Elsevier.

2. Photocatalytic CO_2 Utilisation by MOF Hybrids

2.1. Noble-Metal-Based MOFs

Within the photocatalytic literature, the use of noble metals is ubiquitous. Owing to the ability to harness localised surface plasmonic resonance (LSPR), it is possible to tune the excitation frequencies of noble metal NPs to the visible spectral range through variations in particle size, shape, and dielectric environment [83–88]. The excited plasmons can undergo decay via radiative [89] and non-radiative processes [90]. Radiative decay involves the re-emission of photons, whereas non-radiative decay takes place via the generation of electron–hole pairs (e^-–h^+), known as Landau damping (LD) [83]. LD is a quantum mechanical phenomenon involving the transfer of plasmons into e^-–h^+ pairs within femtoseconds. Additionally, the large-field enhancement effects are also generated inside and near the metal NPs due to the collective electronic oscillations [91,92]. The field enhancement effects have been widely applied in various applications, such as in surface-enhanced Raman scattering (SERS), tip-enhanced Raman scattering (TERS), sensing, and nanophotonics [83]. Plasmonic heating is another possible non-radiative energy dissipation pathway leading to temperature increments of the catalytic system [93,94]. The photo-induced formation of electron–hole pairs makes these NPs ideal candidates for photocatalytic processes, such as the reduction of CO_2 to high-value, renewable fuels such as hydrogen (H_2), methanol, and formic acid [95]. The heterogenisation of MOFs with other catalytically active metal such as Pt and Rh has also been discussed as an effective strategy for the preparation of hybrid photocatalysts for CO_2 utilisation. Within this section, the activities of noble-metal-based photocatalysts will be examined, which are summarised in Table 2 below.

Table 2. Noble metal species incorporated within MOFs for photocatalytic CO_2 utilisation.

MOF Hybrid Photocatalyst	Synthetic Methodology	Light Source	Photoreduction Product	Photocatalytic Performance	Reference
Ag@Co-ZIF-9	In situ reduction	200 W Xe ≥420 nm	CO	CO + H_2 = 102.6 μmol h^{-1}	[96]
Ag@MIL-101-Cr	In situ reduction	300 W Xe 400–780 nm	CO/CH_4	CO = 808.2 μmol $g^{-1}h^{-1}$ CH_4 = 427.5 μmol $g^{-1}h^{-1}$ H_2 = 82.1 μmol $g^{-1}h^{-1}$	[97]
Ag@Co-MOF-74	Solvothermal transformation	300 W Xe 400–1000 nm	CO/H_2	CO ≈ 10 μmolh^{-1} H_2 ≈ 17 μmolh^{-1}	[98]
Au@PPF-3	Dispersion	200 W Xe ≥400 nm	HCOOH	42.3 μmol $g^{-1}h^{-1}$	[99]
Au@TiO_2	Solvothermal/pyrolitic conversion	200 W Hg/Xe 200–750 nm	CH_4	10 ppm/h	[100]
Pt@MIL-125(Ti)	In situ reduction	300 W Xe 420–800 nm	$HCOO^-$	H_2 = 235 μmol $HCOO^-$ = 13 μmol	[101]
Pt@NH_2-UiO-68	Solvothermal	300 W Xe 400–780 nm	CO	400 μmol g^{-1}	[102]
Ag⊂Re_3-MOF	Mixed linker Solvothermal	300 W Xe 400–700 nm	CO	0.093 h^{-1}	[15]
Cp*Rh@UiO-67	Linker Exchange	300 W Xe ≥415 nm	H_2/$HCOO^-$	TON $HCOO^-$ = 47 TON H_2 = 36 $HCOO^-$ + H_2 = 1.2 μmol h^{-1}	[103]

2.1.1. Ag-Based Functionalised MOFs

The introduction of NPs onto MOF architectures can be facilitated through a variety of synthetic strategies, and largely depends on the stability of the MOF towards NP formation conditions. Consideration of the intended site for NPs is important, and timely characterisation is often reported to help ascertain the locations of NPs in terms of whether they reside within the porous frameworks or decorate the outer surfaces. Isolation of NPs within the porous framework is usually achieved through solvothermal methods, by mixing pre-synthesised NPs into the precursor solution containing the metal salts and organic linker. This method "grows" the framework around the NPs, encompassing them within its porous system. Conversely, in situ reduction of NP precursors or the direct deposition of NPs onto MOFs often isolates NPs on the surfaces. The latter of these two strategies provide a less synthetically demanding route for NPs@MOF catalysts, as the former relies heavily on inherent MOF stability towards reductive conditions using borohydrides or H_2.

Min Choi et al. attached a rhenium-based photocentre ($Re^{I}(CO)_3Cl$) to the same bipyridyl dicarboxylic acid linker (ReTC) for mounting within UiO-67 [15]. In the synthesis of the Re_n-framework, a solvothermal protocol was established, in which varying stoichiometric ratios of the bipyridyl and photoactive linker were added to the precursor solution to yield frameworks with varying Re contents (Figure 2a). Under visible light illumination using trimethylamine as a sacrificial electron donor, it was found that the framework consisting of 3 photoactive ReTC linkers per unit cell provided the highest activity for conversion of CO_2 to CO. Structural analysis of the Re_3-MOF showed that the ReTC linkers covalently bound within the octahedral cavities of the framework and adopted a *fac* arrangement about the Re-centre, as confirmed by Fourier difference maps, by IR and NMR imaging, and by the presence of a metal-to-ligand charge-transfer (MLCT) band at 400 nm.

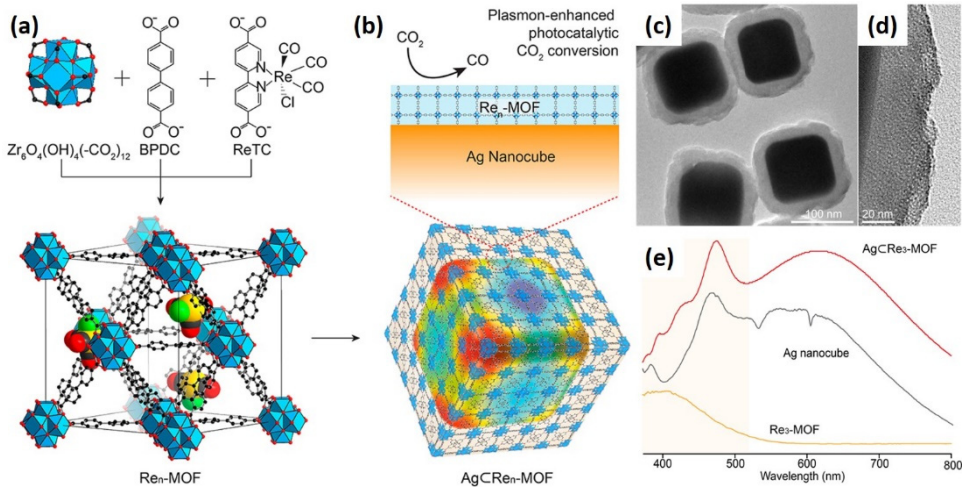

Figure 2. Structures of Re_n-MOF and Ag⊂Re_n-MOF for plasmon-enhanced photocatalytic CO_2 conversion. (**a**) $Zr_6O_4(OH)_4(-CO_2)_{12}$ secondary building units are combined with 4,4′-biphenyldicarboxylate (BPDC) and ReTC linkers to form Re_n-MOF. The structure of Re_3-MOF is shown, as identified from single-crystal X-ray diffraction. The 12-coordinated Zr-based metal clusters are interconnected with 21 BPDC and 3 ReTC linkers in a face-centred cubic array. Atom labeling scheme: C, black; O, red; Zr, blue polyhedral; Re, yellow; Cl, green; H atoms are omitted for clarity. (**b**) Re_n-MOF coated on a Ag nanocube for enhanced photocatalytic conversion of CO_2. (**c**) TEM image of Ag⊂Re_3-MOF, showing Re_3-MOF constructed on the surface of an Ag nanocube. (**d**) Magnified image of Re_3-MOF and (**e**) UV−vis spectra of the Re_3-MOF, Ag nanocube, and Ag⊂Re_3-MOF. Adapted with permission from [15]. Copyright 2017, American Chemical Society.

To further improve the photocatalytic activity, the Re_3-MOF was coupled to the Ag nanocubes to produce a bifunctional catalyst, as shown in Figure 2b. Following the same solvothermal method used to prepare the Re_3-MOF but with the addition of pre-formed Ag nanocubes, the Re_3-MOF was crystallised

around the nanocubes to produce Ag⊂Re_n-MOF, the thickness of which was controlled through the synthesis time. Figure 2c,d display the transmission electron spectroscopy (TEM) image of the Ag⊂Re_3-MOF, in which the Re_3-MOF was constructed on the surface of Ag nanocubes. The maximum absorption in the ultraviolet-visible (UV-vis) spectra of Ag⊂Re_3-MOF compared to the Re_3-MOF and Ag nanocube is also shown in Figure 2e. In a similar manner to NPs, the Ag nanocubes can spatially localise the photoactive Re centres to intensified electric fields at their plasmon resonance frequency, which can be orders of magnitudes higher than the incident electromagnetic field. Under identical photocatalytic conditions, the Ag⊂Re_3-MOF exhibited a 5-fold enhancement of activity over the Re_3-MOF. Notably, Ag nanocubes encapsulated in a thinner MOF layer (16 nm) provided a 7-fold enhancement of the photocatalytic activity (ca. TON = 0.09/hr). This observation was attributed to the exponential decay of the near field from LSPR with increasing distance from the surface of the nanocube. Control experiments using MOF layers with no ReTC (Ag⊂Re_0-MOF) showed no activity, ruling out the possibility of Ag being responsible for CO production. Furthermore, upon coating a similar loading of ReTC onto similar sized Cu NPs, which do not observe LSPR characteristics that match the absorption features of ReTC, activity enhancement was not observed.

Using a photodeposition method to form NPs, Chen et al. decorated cobalt based-zeolitic imidazolate framework (Co-ZIF-9) samples with varying quantities of Ag NPs in order to enhance the previously reported catalytic potential of bare Co-ZIF-9 [104], as well as its capability as a co-catalyst within a cadmium sulfide(CdS)–bypyridine photocatalytic system [96,105]. In the presence of a photosensitiser ($(Ru(bpy)_3)Cl_2 \cdot 6H_2O$) (bpy = 2′,2-bipyridine) and triethanolamine (TEOA), Co-ZIF-9 provided 13.3 and 19.3 μmol of CO and H_2, respectively. Owing to the Co^{2+} centres within the framework, the deep-purple appearance of Co-ZIF-9 provides strong adsorption in the visible spectral range above 500 nm. With the addition of Ag NPs, the absorption range of the hybrid catalyst expanded to include the higher energy wavelengths in the 350–500 nm region. With 2.07 wt % of Ag NPs, an immediate change in selectivity was observed; CO generation increased to 17.2 μmol and H_2 evolution decreased to 14.8 μmol. The optimum wt % of Ag within the framework was found to be 5 wt %. To elucidate the source of the reduction product, Chen et al. [96] conducted an isotopic experiment using carbon-13-labelled CO_2 ($^{13}CO_2$). Under the same reaction conditions, mass spectrometry reported peaks at m/z 29 and 45 only, with no signal detected at m/z 28. This confirmed that the produced CO was the result of successful reduction of the CO_2 feedstock rather than decomposition of other organics within the photocatalytic system.

Through the reduction of an $AgNO_3$ precursor using $NaBH_4$, Guo et al. decorated the external surfaces of pre-formed chromium terephthalate metal-organic framework, MIL-101(Cr) (Matérial Institut Lavoisier) nanocrystals with ~8 nm Ag NPs [97]. Displaying the characteristic deep-green colour of Cr^{3+}, bare MIL-101(Cr) strongly absorbs in the visible region. The MOF decorated with Ag NPs expanded the absorption corresponding to the LSPRs of Ag in the absorption wavelength range into the near-IR region (400–1200 nm), providing a greater coverage of the solar spectrum. By efficiently engineering different sizes of MIL-101(Cr) nanocrystals through varying the MOF-precursor concentrations, Guo et al. effectively demonstrated the crystal-size dependency of the photocatalytic system in the photoreduction of CO_2 to CO, H_2, and CH_4 products. Across a sample range encompassing crystal sizes from 80 to 800 nm, it was shown that the Ag-decorated MIL-101(Cr) catalysts with the smallest crystallite size provided superior catalytic activity in TEAOH, yielding rates of 808.2, 427.5, and 82.1 $\mu mol g^{-1} h^{-1}$ for CO, H_2, and CH_4, respectively. The photoreduction rates using 800 nm crystallites were 23, 18, and 35 times lower than the 80 nm system, respectively. Without the inclusion of Ag NPs, the 80 nm catalysts provided the highest rates for bare MIL-101(Cr) but showed vastly decreased performance when compared to those decorated with Ag NPs. Furthermore, under identical conditions and NP loading, Ag NPs dispersed onto Al_2O_3 provided a very low rate of CO production (8.8 $\mu mol g^{-1} h^{-1}$).

Using a simplified model, the size-dependent activity was attributed to the densities of unit cells on the edges and corners as percentages of the total surface unit cells. For the 80 nm catalyst,

63.6% of surface unit cells within the crystal lie along edges and corners. This percentage significantly decreases with increasing crystal size, with the 800 nm particle displaying only 6.6% of unit cells along edges and corners. This gives rise to favourable photo-responsive properties for the smaller crystallites, providing superior photocurrents under illumination, and concomitantly the lowest electron transfer resistance. Together, the deposition of Ag NPs provides enhanced light adsorption, while size-engineered MIL-101(Cr) facilitates enhanced charge-separation.

Utilising another member of the ZIF-family, Deng et al. utilised a solvothermal treatment of a pre-formed, Ag-NP-decorated Co-ZIF-67 framework with an appropriate linker (2,5-dihydroxyterephthalic acid, H_4DOBDC) in order to induce a transformation to an Ag-NP-functionalised, hollow Co-MOF-74 [98]. Through this novel strategy, Co-MOF-74 particles with a double-layer hollow shell structure were prepared without any remarkable change in the morphology in comparison to original ZIF-67 particles.

Various experiments were conducted by changing the molar ratios of H_4DOBDC to ZIF-67 (n(L)/n(M)) and the concentration of H_4DOBDC (c(L)) to yield hollow shells, as shown in Figure 3. Owing to the cobalt density difference between Co-MOF-74 and Co-ZIF-67 and because H_4DOBDC molecules are bigger than the ZIF-67 channel, the transformation of a ZIF-67 particle to MOF-74 occurs from outside to inside. The low number of Co atoms available to fill in the spaces of the original ZIF-67 particles facilitates the formation of MOF-74's hollow structure. In the instance of higher n(L)/n(M) ratios but low c(L), single-layered hollow structures will be formed. Compared to traditionally synthesised Co-MOF-74 (MOF-74-C), the transformation of ZIF-67 resulted in monodisperse 300 nm particles of Co-MOF-74 (MOF-74-T) composed of ca. 30 nm crystallites. Although providing lower total N_2 adsorption capacity, MOF-74-T gave a much larger external surface area and increased pore volume, which was attributed to the hollow nature of the MOF architecture. To demonstrate the structural advantages of MOF-74-T and AgNPs@MOF-74 compared to the MOF-74-C, the efficiency levels of the co-catalysts were tested in the photocatalytic conversion of CO_2 to CO in the presence of $Ru(bpy)_3Cl_2$ and TEOA. It was found that all catalysts displayed H_2 generation ability, however superior performance was shown by the AgNPs@MOF-74 catalyst (CO = ca. 10 μmol/h, H_2 = ca. 17 μmol/h), which was attributed to the LSPR effect of Ag NPs. MOF-74-T provided decreased activity without decoration of NPs, however still provided better performance than the conventionally crystallised MOF by a factor of 1.8 (MOF-74-T: CO = ca. 4.4 μmol/h, H_2 = ca. 8 μmol/h). Deng et al. [98] concluded that the larger external surface area of the hollow structure leads to the exposure of more co-catalytic active sites, while the thin shell allows diffusion of the reactants and bulky $Ru(bpy)_3Cl_2$.

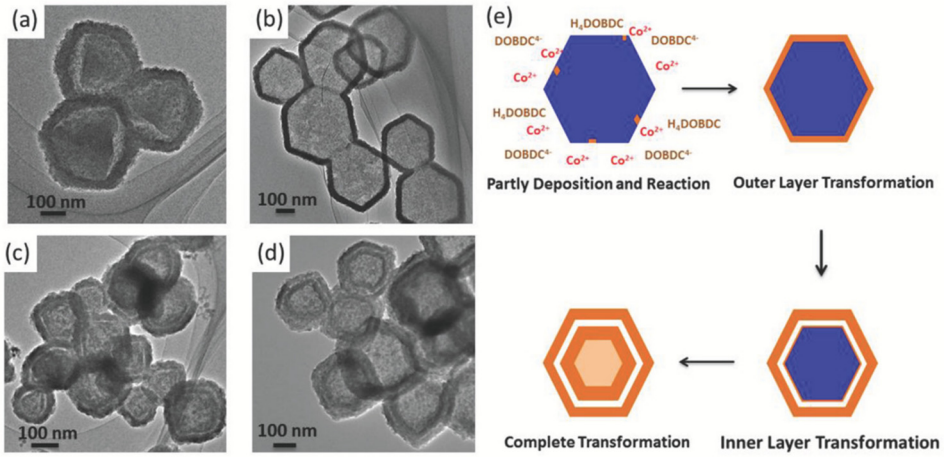

Figure 3. MOF-74-T synthesised in different conditions (L for H_4DOBDC, M for ZIF-67): (**a**) n(L)/n(M) = 0.3, c(L) = 1 × 10 − 3 m; (**b**) n(L)/n(M) = 0.6, c(L) =0.03 × 10 − 3 m; (**c**) c(L) = 0.25 × 10 − 3 m, n(L)/n(M) = 2; (**d**) c(L) = 16.7 × 10 − 3 m, n(L)/n(M) = 2. (**e**) Illustration of the transformation strategy process. Reproduced with permission from [98]. Copyright 2019 Wiley-VCH.

2.1.2. Au-Based Functionalised MOFs

In order to replicate the intriguing catalytic performance of ultra-thin materials, such as carbon-based sheets, metals, and metal dichalcogenides, compared to other heterogeneous morphologies, Chen et al. employed a Co^{2+}-based porphyrin paddle wheel framework (PPF) to host Au NPs [99]. Figure 4a–f display the scanning electron microscopy (SEM), TEM, and atomic force microscopy (AFM) images of PPF and Au–PPF catalysts with different magnifications. To achieve thin sheets, polyvinylpyrrolidone (PVP) was employed as a structure-directing agent (SDA) to restrict growth along the *c*-axis, resulting in square sheets of 1 µm width and 20 nm thickness. Similar synthesis in the absence of SDA resulted in thicker nanosheets (120 nm).

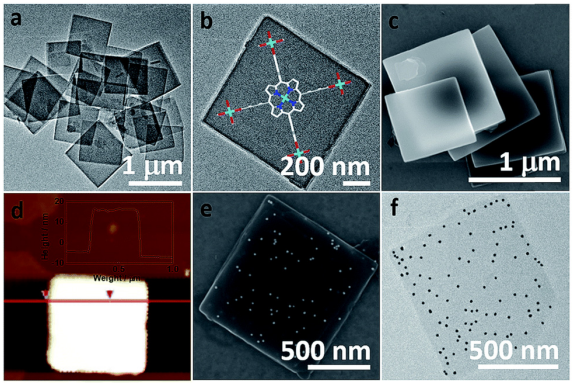

Figure 4. (**a**,**b**) TEM images with different magnifications and (**c**) SEM and (**d**) AFM images of PPF-3_1. (**e**) SEM and (**f**) TEM images of Au–PPF-3_1A. Inset is the profile of a PPF-3_1 nanosheet in the AFM image. Reproduced with permission from [99]. Copyright 2019, the Royal Society of Chemistry.

To decorate the sheets with pre-synthesised Au NPs, Chen et al. [99] added citrate-modified NPs to a dispersion of PPF-3 nanosheets. In order to achieve adequate adhesion between NPs and the PPF-3 sheets, thermal treatment of the PPF-3 in DMF was required. Before washing, it was found that the negative zeta potential of the NPs (−19.4 mV) made it difficult for them to bind to the surface of the PPF-3, which also produced a negative value (−5.9 mV) arising from the surface-bound PVP. Treatment and removal of the SDA shifted the PPF-3 zeta potential to a positive value (+4.9 mV), allowing favourable electrostatic interaction and uniform dispersion across the external surfaces of the PPF-3 sheets. This observation was also partly attributed to the migration of Co^{2+} ions within the PPF-3 sheets.

Using an acetonitrile–ethanol mixture (*v*/*v* = 4:1), the photocatalysts produced formic acid (HCOOH) as the sole product. Both Au-NP-decorated PPF-3 sheets provided higher HCOOH production rates compared to their parent frameworks, with the thin-sheet hybrid providing a superior rate of 42.7 $\mu molg^{-1}h^{-1}$, representing a 5-fold increase in activity compared to the framework without Au NPs (8.3 $\mu molg^{-1}h^{-1}$). Identical catalysis on thicker sheets without NPs provided further inferior activity, clearly demonstrating the importance of the framework thickness to intrinsic electron transfer and mass transport properties. The substitution of ethanol for other aliphatic alcohols such as *n*-propanol and *n*-butanol decreased the rates of HCOOH production to 18.5 and 12.1 $\mu molg^{-1}h^{-1}$, respectively.

Following electro- and photochemical analyses, Chen et al. [99] attributed the activity of the Au NP/PPF-3 system to two factors: (i) upon visible light illumination, electrons from the PPF-3 highest occupied molecular orbital (HOMO) transition to the lowest unoccupied molecular orbital (LUMO) and are transferred to the Co^{2+} centres, generating Co^{+} ions; (ii) deposition of Au NPs amplifies the local electric fields induced by LSPR, resulting in the absorption of more photons and leading to a higher concentration of Co^{+} ions.

Beyond its function as a porous host, Khaletskaya et al. [100] showed amine functionalised-MIL-125 (NH_2-MIL-125(Ti)) to be suitable as a sacrificial precursor for the synthesis of TiO_2. Motivated by the

challenges associated with the controllable production of nanoscale TiO_2 particles and the discernible advantages this can bring to the field of photocatalysis, the pyrolytic conversion of MOF precursors offers routes to unusual metal oxide morphologies, as their porosity provides a host matrix for the loading of additional components [100]. Utilising a solvothermal encapsulation synthesis protocol, Khaletskaya et al. [100] placed pre-formed, monodisperse Au NPs (2.1 ± 0.8 nm) within the precursor MOF solution and heated the resulting mixture to induce crystallisation of the framework. This resulted in a hybrid material for which much larger Au NPs (3.8–20 nm) were identified as residing primarily on the outer surface. Following successful crystallisation, the hybrid MOF was heated in dry O_2 at 450 °C for 2 h to convert the decorated framework into an Au/TiO_2 hybrid. Through this synthetic pathway, 300–450 nm nanocrystals retaining the size and morphology of the host framework were produced, validating the synthetic rationale. A similar process was performed using bare NH_2-MIL-125(Ti) to produce a TiO_2 reference. Notably, analysis by powder X-ray diffraction (PXRD) and Fourier transform (FT) Raman spectroscopy revealed that the presence of Au NPs induced selective crystallisation into the rutile phase, whereas the TiO_2 reference contained traces of anatase [100].

In the photocatalytic formation of CH_4 from a CO_2/H_2O mixture (1.5 and 0.6%, respectively) diluted in He, the Au NP/TiO_2 outperformed the TiO_2 reference catalyst, producing ca. 50 ppm CH_4 across a 6 h reaction. Interestingly, to establish the stability and reusability across subsequent cycles, Khaletskaya et al. [100] observed significant increase in activity for the TiO_2 reference catalyst in the 2nd cycle. Citing similar peculiarities to the work of Strunk et al. [106] on Au/Ti/SBA-15, this observation was attributed to the availability of a residual "carbon pool" on the TiO_2 reference catalyst surface at the beginning of the 2nd cycle [106]. These surface species were generated in the 1st cycle and could not be removed through evacuation between cycles. Consistent CH_4 production was observed for the Au NP/TiO_2 hybrid, which clearly outperformed commercial P25 and AUROlite (commercial Au/TiO_2) [106].

2.1.3. Pt- and Rh-Based Functionalised MOFs

Employing a different member of the MIL family, Sun et al. compared the activity of Pt and Au NPs on NH_2-MIL-125(Ti) for the formation of hydrogen and formate ($HCOO^-$) [101]. MIL-125(Ti) and its amino-based derivative, NH_2-MIL-125(Ti), have been explored extensively for their photocatalytic potential. Reported first by Férey and coworkers, MIL-125(Ti) absorbs strongly in the UV region and has been shown to provide photochromic behaviour when irradiated in the presence of alcohols [107]. To extend the light absorption into the visible region, the terephthalic acid linker was replaced with the amino derivative, 2-aminoterephthalic acid, by Li and co-workers to prepare NH_2-MIL-125(Ti) [108]. In carrying out this substitution, it was found that not only had the absorption properties of the framework been extended into the visible region (Figure 5), the CO_2 sorption capacity had also improved compared to the parent framework.

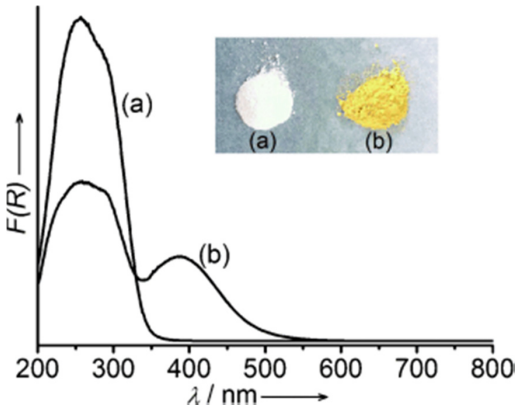

Figure 5. UV-Vis spectra of (**a**) MIL-125(Ti) and (**b**) NH_2-MIL-125 (Ti). The inset shows the samples. Reproduced with permission from [108]. Copyright 2012, Wiley-VCH.

Under visible light irradiation, NH_2-MIL-125(Ti) was shown to be active in the photoreduction of CO_2 to provide $HCOO^-$, whereas the non-substituted framework provided no activity, signifying the importance of the amino group in enhancing the adsorption range of the framework [109]. In the formation of NPs via in situ reduction with H_2, Sun et al. demonstrated that Pt- and Au-NP-deposited NH_2-MIL-125(Ti) samples provide 235 and 40 μmol of H_2, respectively, as the major products over 8 h, whereas no detectable H_2 was observed with NH_2-MIL-125(Ti). This was attributed to the ability of the noble metal NPs to trap excited electrons from the parent framework and provide redox reaction sites for hydrogen evolution. A similar system was demonstrated by Horiuchi et al. using Pt NPs, providing 33 μmol of H_2 after 9 h [110]. Despite this activity, with reference to the previous work by Li and coworkers [108], Sun et al. anticipated a reduction in $HCOO^-$ production upon deposition of noble metal NPs [101]. In the presence of sacrificial electron donor, TEOA, the organic linker within NH_2-MIL-125(Ti), acts as an antenna, transitioning into a long-lived excited charge separation state upon visible light absorption into the ligand-to-metal charge transfer (LMCT) band. This is followed by the transfer of an electron from the organic linker to the metal node. Within these nodes, octomeric Ti-O units ($Ti_8O_8(OH)_4$) are considered as mimics of isolated titanium oxide quantum dots and undergo reduction to the active Ti^{3+} photocatalytic species, producing $HCOO^-$. It was suggested that the noble metal NPs would reduce the possibility of electron transfer to the metal nodes, diminishing the generation of the active Ti^{3+} species. As predicted, under identical photocatalytic conditions, the framework with Au NPs provided a lower $HCOO^-$ (9.06 μmol) yield than the bare NH_2-MIL-125(Ti) (10.75 μmol). The same was not observed for the framework with Pt NPs, however, which provided a 21% increase in activity (12.96 μmol). The use of electron spin resonance (ESR) spectroscopy and DFT calculations revealed that the disparity in activity was attributed to H_2 spillover from the Pt NPs, resulting in the migration of H to corner-sharing oxygen atoms between Ti octahedra, forming Ti^{3+} species. The thermodynamic barrier for this process was calculated to be lower in the case of Pt compared to Au (0.53 vs. 0.94 eV), providing the observed activity [101].

Using an amino derivative of UiO-68(Zr), NH_2-UiO-68, Guo et al. demonstrated the dependence of CO_2 photoreduction performance on the locations of NPs and the lengths of linkers within the MOF hybrids [102]. Contrasting step-wise and one-pot synthesis strategies, Guo et al. deposited Pt NPs (2 wt %) onto the surface (Pt(2)/NH_2-UiO-68) by adding the pre-synthesised MOF into a Pt NP suspension or embedded them within the MOF (Pt(2)@NH_2-UiO-68) via a solvothermal method. Using surface-sensitive, high-resolution X-ray photoelectron spectroscopy (XPS), contrasting Pt peak areas were observed, providing NP locations for catalysts containing equal Pt wt % values, with increased areas observed for surface NPs. The effect of the NP location on the ability of the catalysts to trap electrons was clearly evident during photo and electrochemical measurements, with Pt(2)@NH_2-UiO-68 displaying a 3-fold increase in transient photocurrent response, a significantly smaller capacitance, and an almost fully quenched photoluminescence emission intensity compared to Pt(2)/NH_2-UiO-68. Such observations imply that the position of the Pt NPs has a great influence on the charge separation efficiency in the charge utilisation processes.

In the photoreduction of CO_2 under visible light in the presence of TEOA, CO was produced as the sole product using these catalyst systems. Compared to the bare framework, all Pt NPs containing catalysts provided increased CO production rates. In particular, Pt(2)@NH_2-UiO-68 provided the best performance, displaying a 3-fold enhancement in activity (400.2 $\mu molg^{-1}$) compared to the Pt(2)/NH_2-UiO-68 catalyst with external NPs. This 2 wt % catalyst further outperformed identically synthesised catalysts with loadings of 1 and 4 wt %, as well as a physical mixture of 2 wt % Pt NPs and NH_2-UiO-68 (37.8 $\mu molg^{-1}$), signifying the effect of the NP location on the photocatalytic performance. From these observations and associated Mott–Schottky measurements, Guo et al. [102] suggested that the n-type semiconductor behaviour provided by the NH_2-UiO-68 framework with a 2.87 eV band gap facilitated electron transfer from the framework to the Pt NPs, effectively promoting rapid charge transfer, as illustrated in Figure 6. The location of LUMO of the MOF framework at −0.60 V and the

energy level of Pt at 1.15 V facilitates the efficient electron transfer under visible light irradiation. The electron-rich Pt species exhibit much higher photocatalytic activity in the CO_2 reduction reaction.

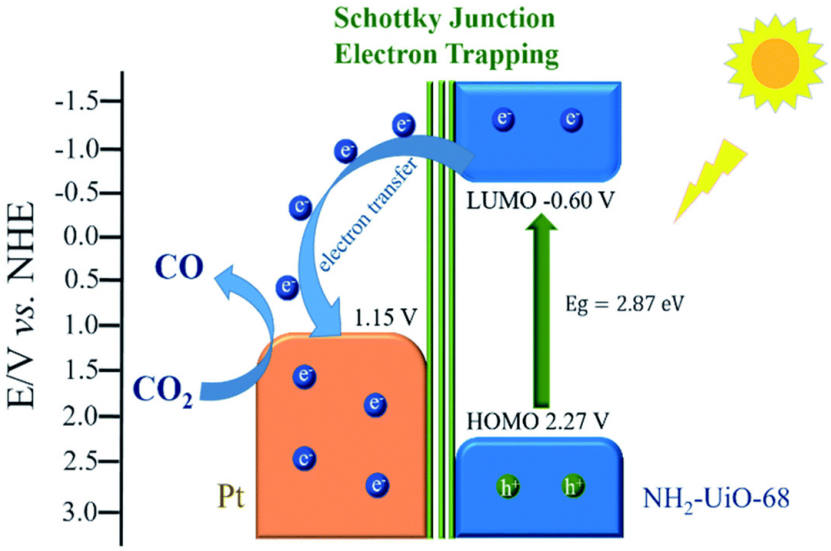

Figure 6. Schematic illustration showing the electron transfer process at the Pt and NH_2-UiO-68 interface based on the energy levels. Reproduced with permission from [102]. Copyright 2019, the Royal Society of Chemistry.

To differentiate the effect of the linker length, an identical catalyst with embedded NPs was synthesised using NH_2-UiO-66 (analogous framework by varying the length of the linker) and tested under identical photo-reductive conditions, providing a reduced yield of CO (102.6 $\mu molg^{-1}$). This observation was attributed to the ability of the NH_2-UiO-68-based framework to accommodate more CO_2 guest molecules.

Aside from the decoration of NPs, another synthetic route for imparting noble-metal-based photocatalytic properties upon a MOF is to mount photoactive moieties onto the organic linker, most commonly performed via PSM procedures. Using UiO-67 as the host framework, Chambers et al. demonstrated this synthetic strategy using a rhodium-based linker modelled upon the biphenyl dicarboxylic acid linker of the original MOF, as illustrated in Scheme 1 [103]. Using a bipyridyl dicarboxylic acid analogue, a photoactive Cp*$RhCl_2$ group (Cp* = pentamethylcyclopendadiene) was bound to the pyridyl nitrogen atoms (CpRh(bpydc)). Owing to the large accommodating pores and inherent stability of the crystallised UiO-67 framework towards moisture and temperature, the framework could undergo post-synthetic ligand exchange, a common synthetic protocol used to insert linkers that would not otherwise crystallise into the framework through traditional solvothermal methods [111]. This process exchanged bound biphenyl linkers with the Cp*Rh linker, heterogenising the photoactive rhodium centre and yielding a series of functionalised, isoreticular MOFs, namely, 5%, 10%, 20%, and 35%-Cp*Rh@UiO-67. Notably, confirming the successful linker exchange, the NMR analysis showed peaks of the displaced biphenyl linker in equivalent stoichiometric quantities. An identical process using a bipyridyl analogue, a linker without dicarboxylic acid groups (CpRh(byr)), provided no such peaks. Although uptake of the CpRh(byr) was observed, it was concluded that it resided within the pores of the framework and could easily be washed out through sequential washing.

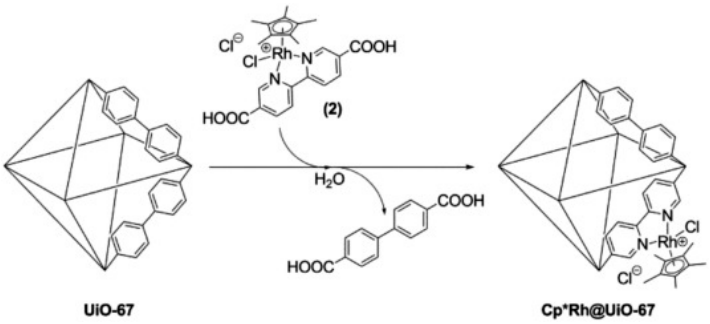

Scheme 1. Heterogenisation of a rhodium complex into the framework of UiO-67 through post-synthetic linker exchange. Reproduced with permission from [103]. Copyright 2015, Wiley.

In establishing the photocatalytic behaviour of the Cp*Rh@UiO-67 in the presence of TEOA and the photosensitiser, $Ru(bpy)_3Cl_2$, the rates of $HCOO^-$ and H_2 generation were compared to that of the homogeneous CpRh(bpydc) linker, as well as the bipyridyl analogue (CpRh(byr)). Other than formate, no other carbon-containing products were detected. In the homogenous phase, CpRh(byr) outperformed CpRh(bpydc) in both $HCOO^-$ and H_2 production (TON[$HCOO^-$] = 125 vs. 42, TON[H_2] = 55 vs. 38, respectively), which was attributed to the electron-withdrawing ancillary carboxylate groups of CpRh(bpydc). Under identical conditions, using a Cp*Rh@UiO-67 framework of near-equivalent Rh loading, the heterogenised catalyst provided comparable performance compared to the homogeneous CpRh(bpydc) (TON[$HCOO^-$] = 47 vs. 42, TON[H_2] = 36 vs. 38, MOF vs. homogeneous). Both systems showed comparable stability over several hours, with a decrease in performance attributed to the breakdown of the photosensitiser rather than the photocatalyst. In particular, the longevity and reusability of the Cp*Rh@UiO-67 was confirmed over 6 cycles, and a cumulative photoactivity in excess of 4 days with only a 20% loss in activity was observed, which was ascribed to continual handling of the catalyst (1.4 mg) and perspective mass losses. Studying the effect of Rh % on catalytic activity, it was found that 10% loading was optimal in the heterogeneous system, beyond which formate production decreased rapidly with concomitant increase in H_2 formation. Above 10% loading in the homogenous system, all activity significantly decreased, suggesting that the heterogenisation procedure provided a stabilisation effect, reducing the possibility of bimetallic deactivation pathways.

Table 3 summarises the MOF hybrid photocatalysts discussed in this section by corelating the specific catalytic descriptors with the observed photocatalytic activity trend, including the crystallite size, nature of the organic linker, surface area, thickness of the MOF framework, location of the NPs, length of the organic linker, and effect of introducing bifunctionality within the MOF framework.

2.2. Non-Noble-Metal-Based MOFs

The use of less expensive non-noble-metals [112–114] such as Co, Ni, Fe, and Cu in MOF photocatalysts with high catalytic activity and selectivity is still a challenge when developing low-cost materials [15,96–98]. It is highly desired to develop cost-effective materials with high performance and durability [115–117], and research efforts have focussed on developing non-noble-metal MOF analogues that rival the catalytic performance of the noble-metal-based counterparts. Much attention has been paid to Fe-containing MOFs, since iron is an earth-abundant element and iron-containing complexes are commonly used in photocatalysis. Further, Fe-based MOF materials are reported to be directly excited by visible light due to the existence of iron-oxo clusters. In particular, terephthalate- and porphyrinic-based Fe-MOFs have seen considerable attention in recent years [118–121]. Table 4 summarises the case studies of Fe-based MOF hybrid photocatalysts discussed in this section.

Table 3. Catalytic descriptors summarising noble metal species incorporated within MOFs for photocatalytic CO_2 utilisation.

Descriptor	MOF Hybrid Photocatalyst	Photocatalytic Trend	Ref
Crystallite size	Ag@MIL-101-Cr	The smallest MIL-101 crystallite decorated with Ag provided superior activity	[97]
Organic linker	Pt@MIL-125(Ti)	The use of 2-aminoterephthalic acid instead of terephthalic acid organic linker enhanced the visible light absorption and CO_2 adsorption capacity	[101]
Surface area and shell thickness	Ag@Co-MOF-74	Large surface area and thin shell allowed exposure to active sites and easy diffusion of substrates, respectively	[98]
NP location	Pt@NH_2-UiO-68	Pt NPs embedded within the MOF displayed 3-fold enhanced activity compared with NPs present on surface	[102]
Length of organic linker	Pt@NH_2-UiO-68	NH_2-UiO-68 gave higher product yields than NH_2-UiO-66 due to its ability to accommodate more CO_2 molecules	[102]
Thickness of framework	Au@PPF-3	Au decorated thin PPF-3 sheets provided superior activity than with thicker sheets	[99]
Bifunctionality	Ag⊂Re_3-MOF	The combination of Re_3-MOF with Ag nanocubes enhanced light absorption and catalytic activity (five-fold) compared with bare Re_3-MOF.	[15]

Table 4. Non-noble-metal species incorporated within MOFs for photocatalytic CO_2 utilisation.

MOF Hybrid Photocatalyst	Synthetic Methodology	Light Source	Photoreduction Product	Photocatalytic Performance	Ref
NH_2-Fe MOFs	Solvothermal	300 W Xe 420–800 nm	$HCOO^-$	178 μmol (8 h)	[118]
Solvent-free NH_2-Fe MOFs	Solvothermal	300 W Xe 420–780 nm	CO	87.6 μmol g^{-1}	[119]
LHP QDs@PCN-221(Fe)	Solvothermal/PSM	300 W Xe ≥400 nm	CO/CH_4	1559 μmolg^{-1} (80 h) CO (34%)/CH_4 (66%)	[121]
In-Fe_xTCPP-MOF	Solvothermal	300 W Xe ≥400 nm	CO	3469 μmolg^{-1} (24 h)	[120]

Acknowledging the difficulties in establishing the photocatalytic processes within NH_2-MIL-125(Ti), Wang et al. reported the photocatalytic performance over three typical Fe-based MOFs and their amino-functionalised derivatives; MIL-101(Fe), MIL-53(Fe), and MIL-88B(Fe) [118]. All three Fe-based MOFs are based upon the terephthalic acid linker bound to Fe-octahedra and the selected MIL frameworks vary only in their topology. MIL-53 is composed of infinite M-OH chains of corner-sharing octahedra bound to four neighbouring chains and is most readily recognised for its associated "breathing" ability. MIL-88B and MIL-101 both share the same trimeric Fe_3O node, within which three metal octahedra are bound by a single bridging μ_3 oxygen molecule and are connected to a further 6 nodes through the terephthalic linker. Similar to MIL-53, MIL-88B shares similar breathing properties and arranges in staggered layers, forming expandable channels upon host incorporation. Conversely, MIL-101 forms a rigid structure with two differently sizes pores composed of hexagonal and pentagonal windows. Through functionalisation with the amino linker derivative, Wang et al. [118] enhanced the absorption of the MOFs within the visible region beyond 700 nm, as well as the adsorption capacity towards CO_2 compared to the unfunctionalised MOFs.

In the presence of TEOA, all functionalised and non-functionalised MOFs reduced CO_2 to $HCOO^-$, with superior activity provided by NH_2-MIL-101(Fe), producing 178 µmol in 8 h. Across the MOF series, Wang et al. [118] demonstrated a linear trend between formate production and CO_2 adsorption, with all amino-functionalised MOFs providing enhanced production compared with their parent framework. Further, using the MIL-101-based frameworks, the reduction process was shown to be photocatalytic in nature, as when a cut-off filter was employed to restrict irradiation wavelengths to above those adsorbed by the non-functionalised framework, $HCOO^-$ was produced, whereas 5.6 µmol of $HCOO^-$ was produced over the amino- derivative. From these observations, Wang et al. concluded that the amino derivative provides an additional excitation pathway for unfunctionalised MOFs, while visible light irradiation results in an excited charge separation state by transferring an electron from the O^{2-} to Fe^{3+} within the metal nodes, generating Fe^{2+}, which is capable of reducing CO_2. For the amino-functionalised derivatives, excitation of the NH_2 functionality followed by an electron transfer from the excited organic linker to the metal centre also generates Fe^{2+}, as shown in Scheme 2. This dual-excitation pathway is similar to that observed for the NH_2-MIL-125(Ti) and NH_2-Uio-66(Zr) frameworks described above [108,122].

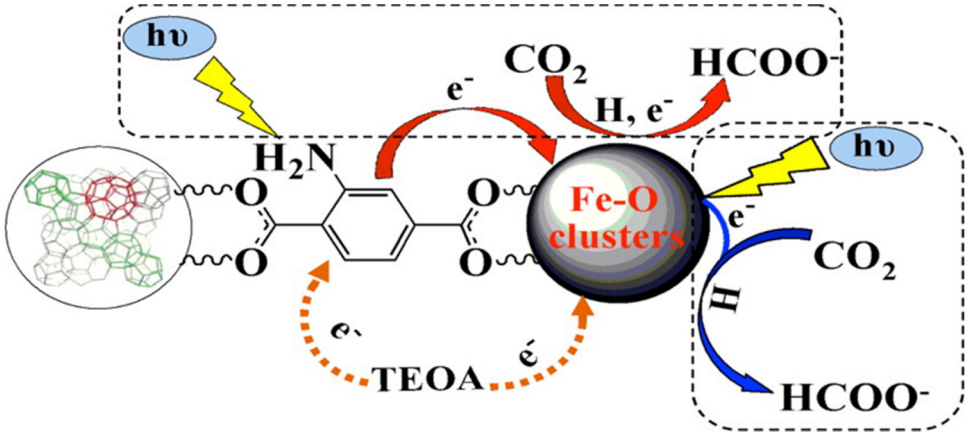

Scheme 2. Scheme for dual-excitation pathways for CO_2 reduction in amine-functionalised, Fe-containing MOFs. Reproduced with permission from [118]. Copyright 2014, American Chemical Society.

Most recently, Dao et al. demonstrated the tuning of selectivity using the same amino-functionalised Fe-MOFs to produce CO by designing a solvent-free system, removing the organic media that are traditionally utilised in photocatalytic reductions, as depicted in Scheme 3 [119]. Within this system, the MOF photocatalyst and TEOA were uniformly dispersed into a glass fibre film. CO_2 gas was pumped into the system and circulated around a pipeline to increase the contact between the catalyst and

CO_2, generating a gas−solid interface. Compared with a conventional gas−liquid−solid reaction route, the solvent-free gas−solid interface removes the organic medium, providing a more environmentally friendly catalysis route and increasing CO_2 adsorption.

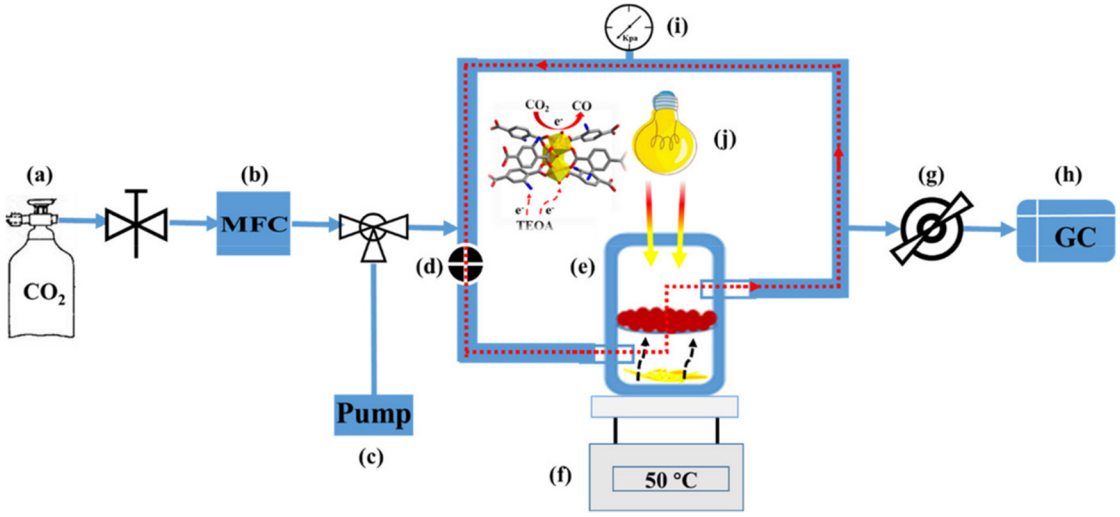

Scheme 3. Schematic of the solvent-free system designed by Dao et al.: (**a**) CO_2 steel cylinder, (**b**) mass flow controller, (**c**) vacuum pump, (**d**) circulating pump, (**e**) photoreactor, (**f**) heating plate, (**g**) automatic gas sampler, (**h**) gas chromatograph, (**i**) pressure meter, and (**j**) light source. Reproduced with permission from [119]. Copyright 2019, American Chemical Society.

Under photocatalytic conditions, all MOFs provided non-linear CO production curves, which were attributed to the high boiling point of TEOA. This facet resulted in slow volatilisation of the TEOA, and therefore little CO generation at the beginning of the cycle. For all experiments, no H_2 or CH_4 gas was evolved and no HCOOH was observed as a liquid product, as determined through NMR. Of the MOFs, NH_2-MIL-101(Fe) provided the best catalytic performance over 5 h, with a CO formation rate of 87.6 $\mu molg^{-1}$, 5.6 times higher than that of the worst performing NH_2-MIL-53(Fe) (15.7 $\mu molg^{-1}$). As previous identified by Wang et al. [118], the superior performance of the MIL-101 framework was attributed to the enhanced CO_2 adsorption capability, as well as coordinatively unsaturated Fe sites within the metal node of the MOF, which become available after removal of pendant H_2O ligands through thermal treatment.

Photoluminescence spectra of the Fe MOFs displayed remarkably decreased fluorescence compared to the amino-functionalised linker, which exhibits an emission at 485 nm. This quenching is attributed to the effective LMCT upon the incorporation of the amino group, and the degree of quenching matches the catalytic trend. Further, using photocurrent measurements, Dao et al. [119] showed that NH_2-MIL-101(Fe) possesses the highest photocurrent, and concomitantly the smallest resistance amongst the tested MOFs, suggesting that the higher catalytic capacity of NH_2-MIL-101(Fe) is attributed to its more efficient charge transfer ability.

Within porphyrinic-based MOF, PCN-221(Fe), Wu et al. encapsulated lead halide perovskite (LHP) quantum dots (QDs) to construct a series of composite photocatalysts of $MAPbI_3$@PCN-221(Fe_x) (x = 0 – 1), as shown in Figure 7 [121]. Based upon 4,4′,4″,4‴-(porphyrin-5,10,15,20-tetrayl) tetrabenzoate] (TCPP) linkers connected by zirconium nodes, the PCN-221 framework provides a unique binding site at the centre of the porphyrin linker to localise a single metal ion. By altering the ratio of bare linkers (H_2TCPP) to metal-containing linkers (TCPP(Fe)), a series of catalysts with varying Fe contents can be synthesised easily. Driven by the improvement in catalytic performance of LHP QDs for converting CO_2 into CO and CH_4 when loaded onto graphene oxide or g-C_3N_4, the strategy employed by Wu et al. [121] was founded upon three considerations: (i) QDs with ultra-small size and homogeneous distribution can be generated in the pores of the MOF; (ii) the MOF framework can provide improved

stability for the LHP QDs, as well as increased catalytic performance; (iii) localisation of the LHP QDs close to the MOFs catalytic centre. The metal ion residing in the TCPP linker shortens the charge transfer distance, enhancing the charge separation efficiency of LHP QDs under visible light irradiation and improving the catalytic activity of the MOFs.

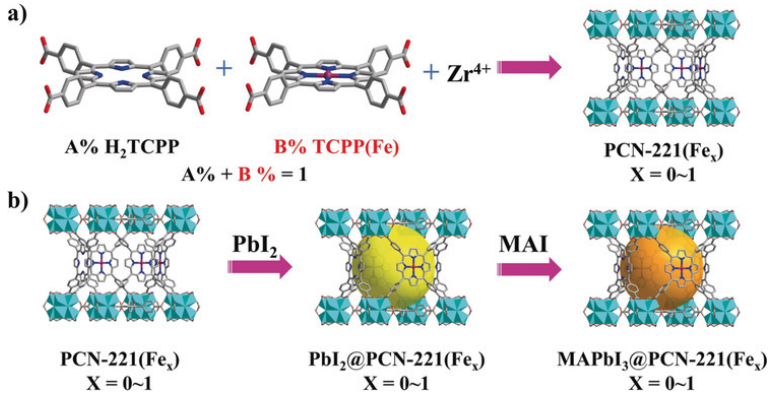

Figure 7. Schematic illustrations of the synthesis of (**a**) PCN-221(Fe_x) and (**b**) $MAPbI_3$ QDs (large spheres) encapsulated in the pores of PCN-221(Fe_x) by a sequential deposition route (MAI = CH_3NH_3I). Reproduced with permission from [121]. Copyright 2019, Wiley-VCH.

To encapsulate QDs into the pores of the MOF, as-prepared PCN-221(Fe_x) was immersed in a PbI_2 solution and then rinsed to remove residual surface PbI_2. The resulting PbI_2@PCN-221(Fe_x) was then immersed in a methyl ammonium iodide (MAI) solution to generate $MAPbI_3$@PCN-221(Fe_x) composite photocatalysts, with QDs of ca. 1.8 nm within the 2 nm pores.

In a CO_2-saturated ethyl acetate solution containing a small amount of water as the sacrificial agent, both QD-decorated and parent framework photocatalysts were tested for the formation of CO and CH_4. Without QDs, the frameworks displayed selectivity for CH_4, whereas CO was the primary product when QDs were encapsulated or frameworks did not include any Fe. No H_2 or liquid products such as HCOOH and CH_3OH were detected for any photocatalytic systems. Without QDs, the yields of CO and CH_4 were 13 and 38 $\mu molg^{-1}$, respectively, after 25 h of irradiation, after which the frameworks were observed to decompose. Under the same conditions, a framework containing QDs but no Fe displayed little activity. With both QDs and Fe ($x < 0$) incorporated into the catalysts, all exhibited significant increases in CO_2 photoreduction activity. Most notably, the photocatalyst containing 20% TCPP(Fe) linker exhibited the highest photocatalytic activity, achieving 104 $\mu molg^{-1}$ of CO and 325 $\mu molg^{-1}$ of CH_4. Furthermore, Wu et al. demonstrated that the encapsulation of LHP QDs provides greater stability to the pristine PCN-221(Fe_x) photocatalyst series, resulting in superior stability of $MAPbI_3$ QDs compared to those reported on other substrates such a ZIFs [16,114,116]. As such, the $MAPbI_3$@PCN-221(Fe_x) photocatalysts display significantly enhanced yields for CO_2 reduction over extended time periods (1559 $\mu molg^{-1}$ over 80 h, CO (34%) and CH_4 (66%)) that are 25–38 times higher than the parent PCN-221(Fe_x) frameworks.

During $^{13}CO_2/H_2{}^{18}O$ isotope trace experiments, mass spectrum signals for ^{13}CO (m/z = 29) and $^{13}CH_4$ (m/z = 17) were observed, indicating that both CO and CH_4 originated from the reduction of CO_2 rather than photo-oxidation of ethyl acetate. Similarly, the evolution of $^{18}O_2$ (m/z = 36) was observed, demonstrating that the water was the reducing agent rather than ethyl acetate. This observation was replicated upon substitution of the ethyl acetate with acetonitrile, for which photocatalytic cycles produced similar amounts of CO, CH_4, and O_2. On the basis of these experiments, Wu et al. highlighted the role this catalytic system can play in the practical application of artificial photosynthesis using water as an electron source.

Most recently, Wang et al. explored a similar methodology to achieve a 2-fold interpenetrated MOF framework containing 4 connected indium nodes and metal-doped porphyrin linkers [120].

The identity of the metal at the centre of the porphyrin linkers, as well as the overall metal content within the linkers, was varied to achieve a series of photocatalysts containing indium (In-InTCPP-MOF), cobalt (In-$Co_{1.71}$TCPP-MOF), or iron (In-Fe_xTCPP-MOF, x = 0.75/1.91/3.56). Utilising XPS measurements, the oxidation states of the Fe and Co ions within the porphyrins were probed. Through identification of the characteristic Fe $2p_{3/2}$ and Fe $2p_{1/2}$ peaks at binding energies of 711.0 and 724.4 eV, respectively, as well as satellite peaks at 719.1 and 728.7 eV, it was concluded that Fe-containing catalysts possessed Fe residing in a Fe(III) oxidation state. For the Co-containing MOF, binding energies of Co $2p_{3/2}$ and Co $2p_{1/2}$ appearing at 780.3 and 795.8 eV, respectively, indicated a Co(II) species in the porphyrin centres. Across all frameworks, In 3d peaks also confirmed the presence of In(III) species.

Within a CO_2-saturated ethyl acetate solution using L-ascorbgyl palmitate (L-AP) as the electron sacrificial agent, the Fe-containing frameworks were found to provide the highest catalytic activity, providing CO as the main product, with only trace amounts of CH_4 (ca. 0.5%) being evolved. After 24 h, no H_2 was detected. From the Fe series, In-$Fe_{1.91}$TCPP-MOF was shown to display the highest catalytic efficiency, with a total CO yield of 3469 $\mu molg^{-1}$ in 24 h. The obtained rate of CO formation indicates the superior activity amongst most noble-metal-free MOF photocatalytic systems. Despite being similar in metal content, the In-$Co_{1.71}$TCPP-MOF provided far less CO, yet outperformed the indium-based framework. The dependence on metal identity was further illustrated by time-resolved PL spectroscopy, as the lifetime was shown to decrease from 0.65 ns for the indium-based framework to 0.19 and 0.38 ns for the Fe- and Co-substituted frameworks, respectively, suggesting rapid electron consumption in the Fe-based system.

Within this system, Wang et al. proposed a mechanistic pathway describing electron transfer from the photoexcited porphyrin linker to the single Fe^{3+} centres, achieving CO_2 reduction. To complete the photocatalytic cycle, the resulting positively charged electron holes oxidize L-AP. This mechanism was supported by calculation of the conduction band (CB, −0.51 V vs. reversible hydrogen electrode (RHE)) potential, which was found to be more negative than that of the standard reduction potential for CO_2 to CO (−0.12 V vs. RHE), thus facilitating CO_2 reduction under visible light. Further, DFT calculations of the CO_2 reduction steps using Fe− and Co−porphyrin analogues showed that the formation of $[Co^{II}(Por^{2-})(COOH^-)]^-$ from $[Co^0(Por)]^{2-}$ is approximately thermoneutral ($\Delta G = -0.25$ kcal mol^{-1}), whereas the same process within Fe analogues was calculated to be more favourable ($\Delta G = -4.10$ kcal mol^{-1}), likely due to the higher stability of $[Fe^{II}(Por^{2-})(COOH^-)]^-$ compared to the corresponding Co analogues.

A summary of catalytic descriptors, including the topology, excitation pathway, presence of unsaturated Fe sites, oxidation state, and proximity of QDs to MOF, has been provided for non-noble-metal functionalised MOFs in Table 5 by linking them with the photocatalytic response observed in the CO_2 utilisation.

2.3. MOFs Incorporated with Miscellaneous Species

The incorporation of transition metals within the MOF architectures has been found to be effective in terms of decreasing the rate of charge recombination and enhancing the charge separation efficiency. However, the high cost and scarcity of some important metals such as Au, Ag, and Ru limits their industrial application. This section covers the miscellaneous species involving carbon-based heterostructures, such as graphene oxide, quantum dots, and carbon nitride, used to develop non-toxic catalysts with enhanced light-harvesting ability. Table 6 enlists the unique catalytic systems that have been developed recently to achieve excellent photocatalytic performances.

Table 5. Catalytic descriptors enlisting non-noble-metal species incorporated within MOFs for photocatalytic CO_2 utilisation.

Descriptor	MOF Hybrid Photocatalyst	Photocatalytic Trend	Ref
Topology	NH_2-Fe MOFs	Three different Fe-based MOFs, namely MIL-101, MIL-53, and MIL-88B, with different topologies and different photocatalytic performances	[118]
Excitation pathway	NH_2-Fe MOFs	Difference in the excitation pathway for amino functionalised and unfunctionalised MOFs under visible light irradiation	[118]
Unsaturated Fe sites	Solvent-free NH_2-Fe MOFs	Thermal treatment removes H_2O ligands and exposes unsaturated Fe sites for enhanced activity	[119]
Proximity (QD to MOF)	LHP QDs@PCN-221(Fe)	Localisation of LHP QDs in close proximity to MOF imparts stability and superior photoreduction ability	[121]
Oxidation state	In-Fe_XTCPP-MOF	The existence of Fe(III) oxidation state in MOF results in the superior photocatalytic reduction	[120]

Table 6. Miscellaneous species incorporated within MOFs for photocatalytic CO_2 utilisation.

MOF Hybrid Photocatalyst	Synthetic Methodology	Light Source	Photoreduction Product	Photocatalytic Performance	Ref
rGO- Ni_3HITP_2	Ultrasonic dispersion	100 W LED 420 nm	CO	TOF = 0.46 min^{-1}; selectivity = 91%	[123]
CD@NH_2-UiO-66	Solvothermal and embedding	Xe Lamp ≥420 nm	CO	16.6 μmol $g_{cat}{}^{-1}h^{-1}$	[124]
g-C_3N_4/ZIF-8	In situ deposition	300 W Xe Full spectrum	CO_2/H_2O to CH_3OH	0.75 μmol h^{-1} g^{-1}	[125]
Morphology-controlled ZIF-67	Solvent-induced method	300 W Xe ≥420 nm	CO	3.89 μmol mg^{-1} h^{-1}	[126]
Single atom/Co-MOF	Wet impregnation	300 W Xe 400–800 nm	CO and CH_4	CO = 200.6 μmol g^{-1} h^{-1} CH_4 = 36.67 μmol g^{-1} h^{-1}	[80]
Co_3O_4 hierarchical nanosheets	Oil bath method and calcination	300 W Xe ≥400 nm	CO and H_2	39.7 μmol h^{-1}	[127]
MOF derived ZnO/NiO porous spheres	Thermal treatment from Zn-Ni MOFs	300 W Xe Full spectrum	CH_3OH	1.57 μmol h^{-1} g^{-1}	[128]

The rational design of multicomponent MOF catalysts by using a carbon-based matrix for enhanced charge transfer was investigated for the first time by Peng et al. [123]. The integration of reduced graphene oxide (rGO) along with a two-dimensional (2D)-MOF (Ni_3HITP_2, HITP = 2,3,6,7,10,11-hexaiminotriphenylene) heterostructure was synthesised via Coulombic and π–π interactions for the photocatalytic CO_2 reduction [123]. The photocatalyst was prepared by dispersing and ultrasonicating the Ni_3HITP_2 MOF in distilled water followed by the addition of rGO under continuous stirring. After vacuum filtration, the composite catalyst, Ni_3HITP_2/rGO, was dried and labelled as NHPG-x, where x = 0.5, 2, and 4, representing the specific amounts of MOF used during synthesis. The fabrication of the heterostructure with rGO assisted in the following ways: (i) the high surface area and conductivity of rGO assisted in the improved charge harvesting; (ii) rGO bridged the efficient charge transfer between catalytic active and light absorption components; (iii) the generation of electronic states enhanced CO_2 activation. The change in the electronic states was studied using XPS and X-ray absorption near edge structure (XANES) spectroscopic analysis. The presence of a shoulder peak at 855.6 eV in the Ni L-edge XANES spectrum for NHPG confirmed the intimate contact between the two components.

The photocatalytic CO_2 reduction reaction was carried out using $[Ru(bpy)_3]^{2+}$, TEOA, and NHPG as the photosensitiser, electron donor, and heterogeneous catalyst, respectively. A superior CO yield of 10.5 $\mu molh^{-1}$ (TOF = 0.46 min^{-1}) over NHPG in comparison to 1.0 $\mu molh^{-1}$ for pure rGO was obtained, along with a high selectivity value of 91.7%. Several control experiments in the absence of light photosensitiser were carried out and CO and H_2 formation was not detected. Moreover, the ^{13}C isotopic studies revealed the formation of ^{13}CO, confirming that the source of CO was from CO_2 and not from other carbon sources, such as TEOA and CH_3CN. The photocatalytic mechanistic pathway for the enhanced CO_2 reduction to CO using NHPG composite films can be summarised in three simple steps: (i) photosensitiser excitation under light irradiation; (ii) photoelectron transfer from rGO to metal active site in the MOF; (iii) CO_2 reduction to CO at Ni-Ni_4 sites. This work is an example of promoting the CO_2 conversion synergistically via improved electron transport and light harvesting through the integration of MOF with the rGO heterostructure.

A similar approach of encapsulating carbon dots (CDs) with the MOF was explored by Li et al. CDs are special nanomaterials with sizes below 10 nm, which also contain various polyaromatic functional groups. They can exhibit strong UV-Vis absorption due to π–π* and n–π* transitions. The NH_2-UiO-66 MOF was integrated with CDs in order to improve the efficiency of the photocatalytic CO_2 reduction [124]. The authors have compared the influence of the encapsulation of CDs within the pores (CD@NH_2-UiO-66) and on the surface of MOFs (CD/NH_2-UiO-66), as illustrated in Scheme 4. The presence of CDs leads to improved charge transfer due to the generation of heterojunctions within the MOFs. This strategy to develop novel MOF hybrid photocatalysts was investigated in the photocatalytic reduction of CO_2 to CO under visible light irradiation conditions. The rate of CO generation with pristine NH_2-UiO-66 was 3.5 $\mu mol\ g_{cat}{}^{-1}h^{-1}$ and for surface-decorated CD/NH_2-UiO-66 was 4.0 $\mu mol\ g_{cat}{}^{-1}h^{-1}$. A significantly superior catalytic yield of 16.6 $\mu mol\ g_{cat}{}^{-1}h^{-1}$ was obtained with embedded CDs in the MOF, which was 4.5 times higher than the pristine NH_2-UiO-66, highlighting the effect of the CD location on MOF photocatalysts. The photocurrent measurements indicated the highest photocurrent value for the embedded samples, highlighting the efficient charge carrier separation in the MOF. The migration of photogenerated electrons from Zr-oxo clusters of MOFs to CDs is faster in the CD@NH_2-UiO-66 catalyst in comparison to the movement of electrons on the surface of the MOF to reach decorated CDs in CD/NH_2-UiO-66. The photocatalyst could be reused ten times without any loss of activity and while maintaining its morphology, as confirmed by SEM and XRD measurements. The incorporation of CDs as electron receptors as well as photosenitisers is an effective strategy for designing and developing photocatalysts for CO_2 utilisation.

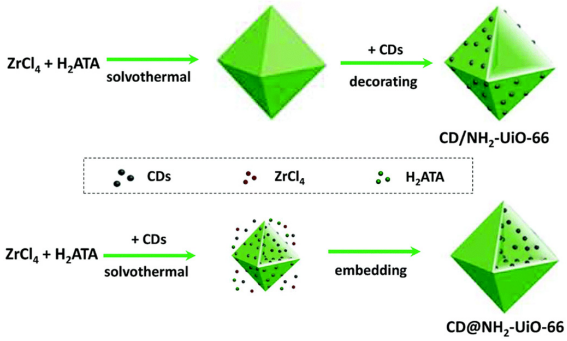

Scheme 4. Schematic illustration of two synthetic routes toward carbon dot (CD)-decorated NH_2-UiO-66 particles and CD-embedded NH_2-UiO-66 particles, respectively. The decoration strategy is based on different surface charges, while the encapsulation strategy is based on using CDs as seeds. Reproduced with permission from [124]. Copyright 2020, the Royal Society of Chemistry.

Graphitic carbon nitride (g-C_3N_4) is one of the most studied photocatalysts for CO_2 reduction under visible light irradiation, but its limited CO_2 adsorption capacity and inferior charge separation ability restrict its use in the design of active photocatalysts. Recently, Liu et al. [125] have explored the cooperative effects of integrating semiconductors with ZIF-8 MOFs to enhance the photocatalytic redox ability, charge separation efficiency, and CO_2 adsorption ability. The decoration of tubular g-C_3N_4 (TCN) with a zeolitic imidazolate framework-8 (ZIF-8) was explored in the CO_2/H_2O vapor to CH_3OH conversion process [125]. The fabrication of photocatalyst was carried out using an in situ deposition method, in which ZIF-8 nanoclusters were grown on the g-C_3N_4 at room temperature. The negatively charged g-C_3N_4 nanotubes have a great affinity for zinc ions, and hence assist in the growth of ZIF-8 nanoclusters without any surface functionalisation. The TEM image of TCN before and after ZIF-8 deposition is shown in Figure 8a,b. To understand the kinetics of the CO_2 reduction reaction, it is essential to study the CO_2 adsorption ability on the surface of the photocatalyst. The linear relationship between the adsorption capacity and relative pressure evidences the interaction between CO_2 and g-C_3N_4/ZIF-8. The photocatalytic CH_3OH production takes place via formation of carbonate, formate, formaldehyde, and methoxy groups, as evidenced by in situ FTIR spectroscopy. Hence, the mechanism for CH_3OH generation was proposed by $2e^-$ and $2H^+$ pathways:

$$CO_2 \rightarrow HCOOH \rightarrow HCHO \rightarrow CH_3OH$$

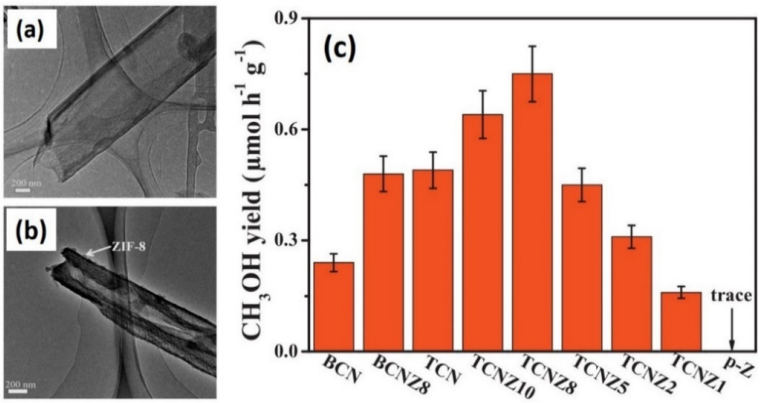

Figure 8. TEM image of (**a**) tubular g-C_3N_4 (TCN), (**b**) tubular g-C_3N_4/ZIF-8 (TCNZ8), and (**c**) photocatalytic generation of CH_3OH over prepared catalysts. Adapted with permission from [125]. Copyright 2017, Elsevier.

Figure 8c displays the obtained catalytic performances for methanol production using various catalysts, including bulk C_3N_4 (BCN), tubular C_3N_4 (TCN), and varied amounts of ZIF-8 on C_3N_4 (TCNZ). The level of methanol generation using the optimal deposition of ZIF-8 on C_3N_4 was three times higher than with the BCN photocatalyst. However, it can be seen that the ZIF-8 had bilateral effects on the CH_3OH generation by enhancing the CO_2 adsorption ability, but the charge transfer was also inhibited due to the poor electrical conductivity of ZIF-8. Hence, it has been demonstrated that reasonable combination and surface functionalisation of TCN photocatalysts can lead to synergetic tuning of photocatalytic processes in the improved conversion of CO_2 to CH_3OH.

Sun et al. studied the effects of different morphologies of ZIF-67 synthesised using the solvent-induced method with different volume ratios of methanol and water in the photocatalytic reduction of CO_2 to CO [126]. The three different morphologies, namely rhombic dodecahedral, pitaya-like, and 2D leaf-like, were labelled as ZIF-67_1, ZIF-67_2, and ZIF-67_3, respectively. The optical responses of the MOF materials were measured together with the photosensitiser $[Ru(bpy)_3]Cl_2{\cdot}6H_2O$ to understand the electronic properties. The absorption within the range of 400–700 nm was associated with the LMCT, depicting the light harvesting ability from blue to red regions of the spectrum. The CO_2 adsorption capability was also investigated for the morphology-controlled ZIF-67 materials. ZIF-67_3 had the smallest surface area and exhibited the maximum CO_2 adsorption value of 1.16 mmol g^{-1}. This was attributed to the (i) presence of flexible cavities between the 2D layers and (ii) strong interactions between the CO_2 and the linker. The photocatalytic CO_2 reduction to CO was performed in the presence of the photosensitiser and with TEOA as the electron donor. Again, ZIF-67_3, having a leaf-like morphology, displayed superior catalytic performance of 3.89 μmol mg^{-1} h^{-1} under visible light irradiation when compared to the values of 3.75 μmol mg^{-1} h^{-1} for ZIF-67_1 and 3.06 μmol mg^{-1} h^{-1} for ZIF-67_2.

A plausible reaction mechanism was proposed, as shown in Figure 9, which was further supported by various operating techniques, including photoluminescence and femtosecond transient absorption spectroscopy. Under visible light irradiation, the excited photosensitiser generates electron–hole pairs at the interface of ZIF-67_3 and $[Ru(bpy)_3]^{2+}$. The electrons are then subsequently transferred to the ZIF-67_3 and TEOA to form $[ZIF\text{-}67\_3]^{-1}$ and $TEOA^+$, respectively. The electrons stored in $[ZIF\text{-}67\_3]^{-1}$ further migrate to CO_2 molecules and assist in the formation of CO.

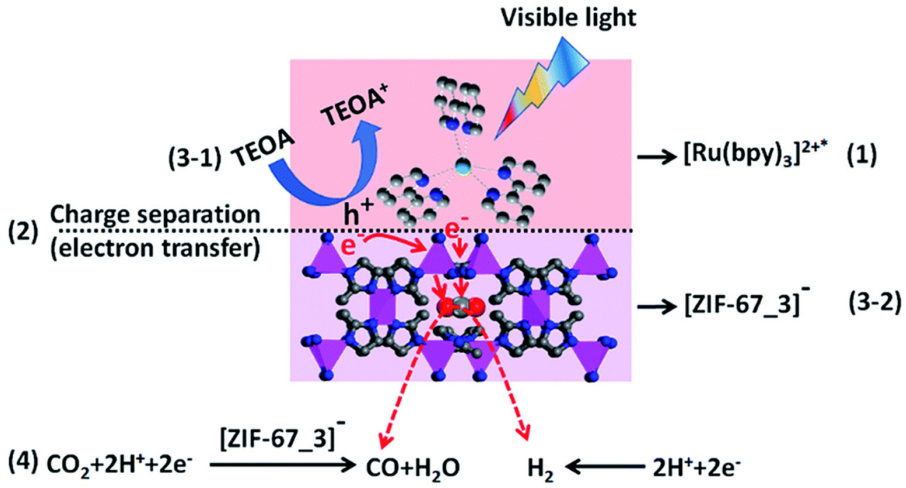

Figure 9. Possible reaction mechanism for the ZIF-67_3 co-catalysed photoreduction of CO_2 by employing $[Ru(bpy)_3]^{2+}$ and TEOA as the photosensitiser and electron donor, respectively. Reproduced with permission from [126]. Copyright 2018, the Royal Society of Chemistry.

The incorporation of single atoms within the framework is still a challenge because of their tendency to aggregate under reaction conditions. Ye et al. explored the incorporation of single Co atoms implanted within the MOF network and investigated the charge separation efficiency in the

porphyrin unit of MOF-525 [80]. In this report, MOF-525, elaborated as $Zr_6O_4(OH)_4(TCPP\text{-}H_2)_3$, was selected as the framework to incorporate Co single-atom species in the porphyrin unit to form MOF-525-Co. The existence of mononuclear centres of Co was confirmed by the extended X-ray absorption fine structure (EXAFS) spectroscopy. The photocatalytic performance was evaluated under visible light irradiation in the presence of TEOA as an electron donor for CO_2 reduction to CO and CH_4. The superior catalytic performance of MOF-525-Co with CO and CH_4 evolution rates of 200.6 and 36.76 μmol g^{-1} h^{-1}, respectively, was compared with MOF-525-Zn, bare MOF-525, and the H_6TCPP ligand. Approximately 3- and 6-fold enhancements of the CO and CH_4 evolution values were obtained for MOF-525-Co compared to MOF-525. This was attributed to a higher CO_2 uptake capacity because of an increase in the number of affinity sites after metallisation of MOF-525. It was also demonstrated by experimental investigation and theoretical simulations that the photogenerated electrons could be easily transferred to the active site in MOF-525-Co, leading to the improved charge separation efficiency. Furthermore, Co-incorporated MOF-525 displayed excellent stability at 3 catalytic cycles without any significant loss of activity.

Apart from implanting various species within the MOFs [129,130], many research groups have developed novel materials derived from several monometallic and bimetallic metal–organic frameworks [122,131]. For example, Zhang et al. synthesised cobalt tetraoxide (Co_3O_4) hierarchical nanosheets (HNSs) via two-step synthesis, involving the preparation of Co-MOF using 1,4-naphthalenedicarboxylic acid as the organic linker followed by calcination (Scheme 5) [127]. Interestingly, when the isophthalic acid (H_2IPA) was used as the organic linker, nanoballs of Co_3O_4 were formed, which ultimately formed NPs after thermal treatment. The 2D morphology of HNSs was confirmed by SEM images, as shown in Figure 10a,b. The TEM images revealed the existence of smaller particles sized 10–20 nm, as shown in Figure 10c–e.

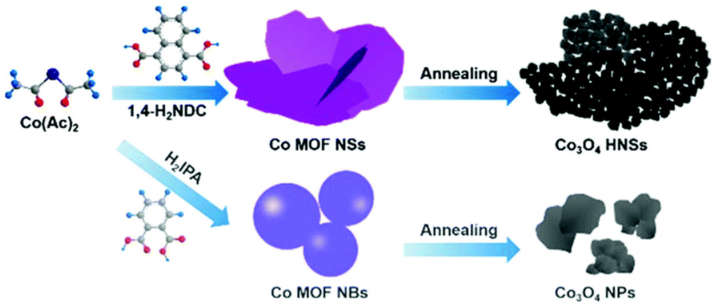

Scheme 5. Schematic illustration of the synthesis process of Co_3O_4 hierarchical nanosheets and Co_3O_4 NPs from the Co MOF. Reproduced with permission from [127]. Copyright 2020, the Royal Society of Chemistry.

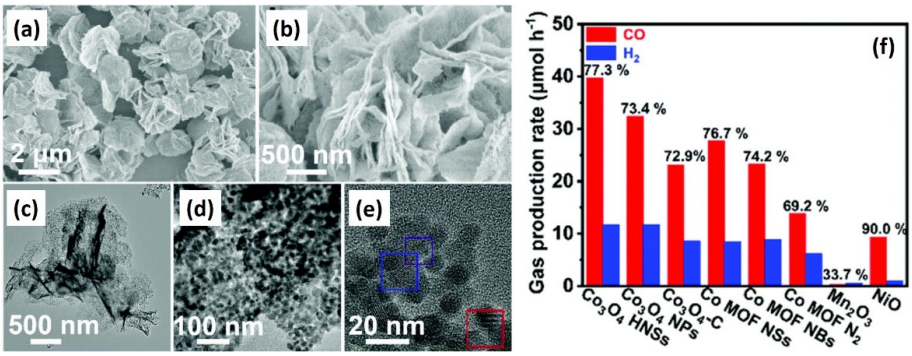

Figure 10. (**a**,**b**) SEM, (**c**–**e**) TEM, and (**f**) photocatalytic reduction of CO_2 to CO and H_2 over different catalysts. Note: Co_3O_4-C stands for commercial Co_3O_4 and Co_3O_4-N_2 refers to the N_2 annealing product Co MOF NSs. Adapted with permission from [127]. Copyright 2020, the Royal Society of Chemistry.

The photocatalytic performance and selectivity of CO generation using Co_3O_4 HNSs was compared with Co_3O_4 NPs and the commercial Co_3O_4, as summarised in Figure 10f. The most frequently used components, $[Ru(bpy)_3]Cl_2 \cdot 6H_2O$ and TEOA, were employed as the photosenitiser and the sacrificial agent for the reaction, respectively. As shown, the Co_3O_4 HNSs displayed superior activity and selectivity of 39.7 μmol h^{-1} and 77%, respectively, under visible light irradiation. The apparent quantum efficiency (AQE) for CO generation was found to be 0.42% at light irradiation value of 450 nm. Several control experiments were carried out, including ^{13}C isotopic studies to confirm the origin of CO as being from CO_2 and not from other carbon sources. No CO or H_2 formation was observed in the absence of a photosensitiser, TEOA, or visible light irradiation, suggesting their significance in obtaining superior photocatalytic performance. One of the major drawbacks of MOFs is their lack of reusability in practical applications. Herein, the Co_3O_4 HNSs derived from Co-MOF was found to be stable without any loss of catalytic activity, even after 4 runs. The authors explained the contribution of HNSs to the excellent catalytic performance as being due to two aspects: (i) the formation of HNSs derived from an MOF with higher surface area values, a mesoporous structure, and better CO_2 adsorption capacity; (ii) the formation of small NPs with narrow size distribution and fewer oxygen vacancies, leading to improved charge separation and migration efficiency under visible light irradiation.

Similarly, Chen and co-workers developed an MOF-derived photocatalyst for improved photocatalytic performance for CO_2 conversion to CH_3OH. They synthesised ZnO/NiO porous hollow spheres through the thermal treatment of Ni-Zn bimetallic organic frameworks (MOFs) [128]. It has been reported that hollow structures can enhance the light absorption ability because of the multiscattering effect and that the porous structure can lead to a high surface area, increased CO_2 adsorption capacity, and improved photocatalytic performance. The decomposition of bimetallic MOFs leads to the homogeneous mixing of n-type ZnO and p-type NiO, leading to the formation of p-n heterojunctions within the hybrid material. The obtained hollow spheres were labeled as ZN-10, ZN-30, and ZN-50 based on the differences in the amounts of precursor solution used in the synthesis. The XPS studies revealed the transfer of electrons from ZnO to NiO in the composite, further assisting in improving the charge separation efficiency. The photocatalytic CO_2 reduction to CH_3OH over ZN-X hollow spheres was compared with pristine ZnO and NiO metal oxides. The relatively low amounts of CH_3OH generation on ZnO (0.6 μmol h^{-1} g^{-1}) and NiO (negligible) suggested that pure oxides are not active under the given experimental conditions. However, all ZnO/NiO composites were found be active and a superior catalytic performance was shown by ZN-30 (1.57 μmol h^{-1} g^{-1}), which was three times greater than results obtained over ZnO. The excess amounts of NiO in the catalyst can restrict the light absorption ability and may also have acted as the charge recombination centre that led to the decrease in the photocatalytic activity of ZN-50.

Table 7 lists information on the catalytic descriptors discussed in this section, including the surface area, number of affinity sites, organic linker, effect of morphology, and location of CDs for miscellaneous species incorporated into MOFs in photocatalytic CO_2 utilisation.

Table 7. Various catalytic descriptors summarising the photocatalytic trends in the miscellaneous species incorporated into MOFs for CO_2 utilisation.

Descriptor	Photocatalyst	Photocatalytic Trends	Ref
Surface area	rGO- Ni_3HITP_2	rGO heterostructure creating high surface area and enhanced conductivity	[123]
Location of CDs (carbon dots)	CD@NH_2-UiO-66	An approximately 4 times higher catalytic yield with embedded CDs than surface decoration	[124]
Affinity sites	g-C_3N_4/ZIF-8	Negatively charged g-C_3N_4 provided affinity to Zn ions for the growth of ZIF-8 nanoclusters	[125]
	Single atom/Co-MOF	Co metallisation increasing the number of affinity sites in MOF-525 for CO_2 adsorption	[80]
Synergistic interaction	g-C_3N_4/ZIF-8	Improved CO_2 conversion due to synergistic tuning between g-C_3N_4 and ZIF-8	[125]
Morphology vs. surface area	Morphology-controlled ZIF-67	Smallest surface area for 2D leaf-like ZIF-67 with maximum CO_2 adsorption because of flexible cavities absent in rhombic and pitaya-like morphologies	[126]
Organic linker vs. morphology	Co_3O_4 hierarchical nanosheets (HNSs)	The use of 1,4-naphthalenedicarboxylic acid as organic linker formed Co_3O_4 HNSs and isophthalic acid formed Co_3O_4 NPs	[127]
NPs size vs. distribution	Co_3O_4 hierarchical nanosheets (HNSs)	Small NPs of HNSs with narrow size distribution enhanced migration efficiency	[127]
Monometallic vs. bimetallic	MOF derived ZnO/NiO porous spheres	Bimetallic ZnO/NiO MOFs exhibited three times greater yield than ZnO or NiO oxides	[128]

3. Summary and Outlook

In summary, we have compared and contrasted the photocatalytic CO_2 reduction of three different types of MOF-based hybrid materials functionalised by (i) noble metal NPs (Ag, Au, Pd, Ru), (ii) non-noble-metal NPs (Fe, Co), and (iii) miscellaneous species, including carbon dots, r-graphene oxide, and g-C_3N_4. These MOF-based hybrid systems, along with their photocatalytic performances, have been listed in Tables 2, 4 and 6. Moreover, we have linked specific catalytic descriptors to the observed photocatalytic trends at the end of each section (Tables 3, 5 and 7). For example, the size of MOF crystallites can significantly impact the photocatalytic performance. The choice and length of an appropriate organic linker, the location of NPs, the surface area, and the oxidation state have been discussed, corelating the trends observed in the photocatalytic CO_2 reduction. The higher surface area of MOFs and their ability to tune the porosity, metal centres, and organic ligands are the reasons for their unique flexibility in various applications, such as in drug delivery, gas sorption, CO_2 capture, and sensing. These versatile structural properties enable photocatalytic applications in hydrogen generation, CO_2 reduction, pollutant degradation, and several organic transformation reactions. The functionalisation of MOFs by metal substitution and the integration of photo-sensitive components or semiconductors assist in improving the visible light harvesting and CO_2 conversion efficiency. We also discussed the preparative techniques and factors affecting the introduction of multifunctionalities within the MOF framework, such as carbon dots, single atoms, quantum dots, and g-C_3N_4 semiconductors, in enhancing the overall conversion efficiency. MOFs are emerging heterogeneous photocatalysts that are used for CO_2 reduction, especially because of their excellent CO_2 capture capacities.

Despite great progress being made in the design and development of MOF-based photocatalysts for CO_2 reduction, there are still some challenges and limitations in achieving artificial photosynthesis in practical applications. Owing to the organic nature of the linkers, MOFs have much lower stability toward temperature, pressure, moisture, and pH than other zeo-type materials. Many MOFs breakdown at temperatures above 350 °C, dramatically reducing the number of applications. Due to this, MOFs must be considered for more niche, lower temperature syntheses, such as fine chemical synthesis, which can utilise their shape-specific topologies and high metal contents. MOFs have various limitations, including their fast recombination of charge carriers, limited absorption in the visible light region, and complex photocatalytic mechanisms involved in the reduction reaction. The main concern regarding the use of MOFs in the photocatalytic reduction of CO_2 is the small amounts of products formed, which restricts their industrial application. The photocatalytic stability is another important issue faced by materials scientists in maintaining the number of recycling test runs. Many research reports have demonstrated the superior photocatalytic performance of MOFs when compared with inorganic semiconductors; however, continuous decreases in activity during recycling tests have hindered their large-scale use. The reports summarised here include the use of sacrificial reagents to carry out photocatalytic reduction, which are expensive and detrimental to the environment. Research efforts are required to overcome the use of such additional sacrificial reagents. The investigation of photocatalytic CO_2 reduction is still at an early stage and we predict that this article will further assist in providing timely progress and guidelines for the design of photoactive MOF-based catalysts for CO_2 reduction. We look forward to major advancements in this field for practical applications.

Author Contributions: Conceptualisation, P.V. and R.R.; writing—P.V. and D.J.S.; writing—review and editing, P.V., D.J.S., and R.R.; supervision, R.R. All authors have read and agreed to the published version of the manuscript.

Funding: This research received no external funding.

Acknowledgments: P.V. would like to acknowledge the Royal Society—Newton International Fellowship for her postdoctoral research funding (NIF\R1\180185) at University of Southampton.

Conflicts of Interest: The authors declare no conflict of interest.

References

1. Izumi, Y. Recent advances in the photocatalytic conversion of carbon dioxide to fuels with water and/or hydrogen using solar energy and beyond. *Coord. Chem. Rev.* **2013**, *257*, 171–186. [CrossRef]
2. Tu, W.; Zhou, Y.; Zou, Z. Photocatalytic conversion of CO_2 into renewable hydrocarbon fuels: State-of-the-art accomplishment, challenges, and prospects. *Adv. Mater.* **2014**, *26*, 4607–4626. [PubMed]
3. Gibbins, J.; Chalmers, H. Carbon capture and storage. *Energy Policy* **2008**, *36*, 4317–4322. [CrossRef]
4. Bui, M.; Adjiman, C.S.; Bardow, A.; Anthony, E.J.; Boston, A.; Brown, S.; Fennell, P.S.; Fuss, S.; Galindo, A.; Hackett, L.A.; et al. Carbon capture and storage (CCS): The way forward. *Energy Environ. Sci.* **2018**, *11*, 1062–1176.
5. Pires, J.C.M.; Martins, F.G.; Alvim-Ferraz, M.C.M.; Simões, M. Recent developments on carbon capture and storage: An overview. *Chem. Eng. Res. Des.* **2011**, *89*, 1446–1460. [CrossRef]
6. Raman, S.K.; Raja, R.; Arnold, P.L.; Davidson, M.G.; Williams, C.K. Waste not, want not: CO_2 (re)cycling into block polymers. *Chem. Commun.* **2019**, *55*, 7315–7318. [CrossRef]
7. Liu, G.; Hoivik, N.; Wang, K.; Jakobsen, H. Engineering TiO_2 nanomaterials for CO_2 conversion/solar fuels. *Sol. Energy Mater. Sol. Cells* **2012**, *105*, 53–68. [CrossRef]
8. Tahir, M.; Amin, N.S. Advances in visible light responsive titanium oxide-based photocatalysts for CO_2 conversion to hydrocarbon fuels. *Energy Convers. Manag.* **2013**, *76*, 194–214. [CrossRef]
9. Kondratenko, E.V.; Mul, G.; Baltrusaitis, J.; Larrazábal, G.O.; Pérez-Ramírez, J. Status and perspectives of CO_2 conversion into fuels and chemicals by catalytic, photocatalytic and electrocatalytic processes. *Energy Environ. Sci.* **2013**, *6*, 3112–3135.
10. Fu, J.; Zhu, B.; Jiang, C.; Cheng, B.; You, W.; Yu, J. Hierarchical Porous O-Doped g-C_3N_4 with Enhanced Photocatalytic CO_2 Reduction Activity. *Small* **2017**, *13*, 1–9. [CrossRef]
11. Yu, J.; Low, J.; Xiao, W.; Zhou, P.; Jaroniec, M. Enhanced photocatalytic CO_2-Reduction activity of anatase TiO_2 by Coexposed {001} and {101} facets. *J. Am. Chem. Soc.* **2014**, *136*, 8839–8842. [CrossRef] [PubMed]
12. Jiang, Z.; Wan, W.; Li, H.; Yuan, S.; Zhao, H.; Wong, P.K. A Hierarchical Z-Scheme α-Fe_2O_3/g-C_3N_4 Hybrid for Enhanced Photocatalytic CO_2 Reduction. *Adv. Mater.* **2018**, *30*, 1–9. [CrossRef] [PubMed]
13. Meng, A.; Zhang, L.; Cheng, B.; Yu, J. TiO_2 -MnO_x -Pt Hybrid Multiheterojunction Film Photocatalyst with Enhanced Photocatalytic CO_2 -Reduction Activity. *ACS Appl. Mater. Interfaces* **2019**, *11*, 5581–5589. [CrossRef] [PubMed]
14. Nie, N.; Zhang, L.; Fu, J.; Cheng, B.; Yu, J. Self-assembled hierarchical direct Z-scheme g-C_3N_4 /ZnO microspheres with enhanced photocatalytic CO_2 reduction performance. *Appl. Surf. Sci.* **2018**, *441*, 12–22.
15. Choi, K.M.; Kim, D.; Rungtaweevoranit, B.; Trickett, C.A.; Barmanbek, J.T.D.; Alshammari, A.S.; Yang, P.; Yaghi, O.M. Plasmon-enhanced photocatalytic CO_2 conversion within metal-organic frameworks under visible light. *J. Am. Chem. Soc.* **2017**, *139*, 356–362. [CrossRef] [PubMed]
16. Ou, M.; Tu, W.; Yin, S.; Xing, W.; Wu, S.; Wang, H.; Wan, S.; Zhong, Q.; Xu, R. Amino-Assisted Anchoring of $CsPbBr_3$ Perovskite Quantum Dots on Porous g-C_3N_4 for Enhanced Photocatalytic CO_2 Reduction. *Angew. Chem. Int. Ed.* **2018**, *130*, 13758–13762. [CrossRef]
17. Li, K.; Peng, B.; Peng, T. Recent Advances in Heterogeneous Photocatalytic CO_2 Conversion to Solar Fuels. *ACS Catal.* **2016**, *6*, 7485–7527.
18. Wang, C.C.; Zhang, Y.Q.; Li, J.; Wang, P. Photocatalytic CO_2 reduction in metal-organic frameworks: A mini review. *J. Mol. Struct.* **2015**, *1083*, 127–136. [CrossRef]
19. Zhu, Z.; Qin, J.; Jiang, M.; Ding, Z.; Hou, Y. Enhanced selective photocatalytic CO_2 reduction into CO over Ag/CdS nanocomposites under visible light. *Appl. Surf. Sci.* **2017**, *391*, 572–579. [CrossRef]
20. Tahir, M.; Tahir, B.; Amin, N.A.S. Gold-nanoparticle-modified TiO_2 nanowires for plasmon-enhanced photocatalytic CO_2 reduction with H_2 under visible light irradiation. *Appl. Surf. Sci.* **2015**, *356*, 1289–1299. [CrossRef]
21. Wan, S.; Chen, M.; Ou, M.; Zhong, Q. Plasmonic Ag nanoparticles decorated $SrTiO_3$ nanocubes for enhanced photocatalytic CO_2 reduction and H_2 evolution under visible light irradiation. *J. CO2 Util.* **2019**, *33*, 357–364. [CrossRef]
22. Kuriki, R.; Sekizawa, K.; Ishitani, O.; Maeda, K. Visible-light-driven CO_2 reduction with carbon nitride: Enhancing the activity of ruthenium catalysts. *Angew. Chem. Int. Ed.* **2015**, *54*, 2406–2409. [CrossRef] [PubMed]

23. Yoshida, T.; Yamaguchi, A.; Umezawa, N.; Miyauchi, M. Photocatalytic CO_2 Reduction Using a Pristine Cu_2ZnSnS_4 Film Electrode under Visible Light Irradiation. *J. Phys. Chem. C* **2018**, *122*, 21695–21702. [CrossRef]
24. Huang, P.; Huang, J.; Pantovich, S.A.; Carl, A.D.; Fenton, T.G.; Caputo, C.A.; Grimm, R.L.; Frenkel, A.I.; Li, G. Selective CO_2 Reduction Catalyzed by Single Cobalt Sites on Carbon Nitride under Visible-Light Irradiation. *J. Am. Chem. Soc.* **2018**, *140*, 16042–16047. [CrossRef]
25. Potter, M.E.; Stewart, D.J.; Oakley, A.E.; Boardman, R.P.; Bradley, T.; Sazio, P.J.A.; Raja, R. Combining Photocatalysis and Optical Fiber Technology toward Improved Microreactor Design for Hydrogen Generation with Metallic Nanoparticles. *ACS Photonics* **2020**, *7*, 714–722. [CrossRef]
26. Zhao, J.; Yang, Q.; Shi, R.; Waterhouse, G.I.N.; Zhang, X.; Wu, L.-Z.; Tung, C.-H.; Zhang, T. FeO–CeO_2 nanocomposites: An efficient and highly selective catalyst system for photothermal CO_2 reduction to CO. *NPG Asia Mater.* **2020**, *12*, 1–9. [CrossRef]
27. Yu, F.; Wang, C.; Ma, H.; Song, M.; Li, D.; Li, Y.; Li, S.; Zhang, X.; Liu, Y. Revisiting Pt/TiO_2 photocatalysts for thermally assisted photocatalytic reduction of CO_2. *Nanoscale* **2020**, *12*, 7000–7010. [CrossRef]
28. Yan, J.; Wang, C.; Ma, H.; Li, Y.; Liu, Y.; Suzuki, N.; Terashima, C.; Fujishima, A.; Zhang, X. Photothermal synergic enhancement of direct Z-scheme behavior of $Bi_4TaO_8Cl/W_{18}O_{49}$ heterostructure for CO_2 reduction. *Appl. Catal. B Environ.* **2020**, *268*, 118401–118416. [CrossRef]
29. Xu, M.; Hu, X.; Wang, S.; Yu, J.; Zhu, D.; Wang, J. Photothermal effect promoting CO_2 conversion over composite photocatalyst with high graphene content. *J. Catal.* **2019**, *377*, 652–661. [CrossRef]
30. Wang, L.; Dong, Y.; Yan, T.; Hu, Z.; Jelle, A.A.; Meira, D.M.; Duchesne, P.N.; Loh, J.Y.Y.; Qiu, C.; Storey, E.E.; et al. Black indium oxide a photothermal CO_2 hydrogenation catalyst. *Nat. Commun.* **2020**, *11*, 1–8.
31. Mohan, A.; Ulmer, U.; Hurtado, L.; Loh, J.; Li, Y.F.; Tountas, A.A.; Krevert, C.; Chan, C.; Liang, Y.; Brodersen, P.; et al. Hybrid Photo-and Thermal Catalyst System for Continuous CO_2 Reduction. *ACS Appl. Mater. Interfaces* **2020**, *12*, 33613–33620. [CrossRef] [PubMed]
32. Lee, J.; Farha, O.K.; Roberts, J.; Scheidt, K.A.; Nguyen, S.T.; Hupp, J.T. Metal-organic framework materials as catalysts. *Chem. Soc. Rev.* **2009**, *38*, 1450–1459. [CrossRef] [PubMed]
33. Yaghi, O.M.; Li, H. Hydrothermal Synthesis of a Metal-Organic Framework Containing Large Rectangular Channels. *J. Am. Chem. Soc.* **1995**, *117*, 10401–10402. [CrossRef]
34. Kreno, L.E.; Leong, K.; Farha, O.K.; Allendorf, M.; Van Duyne, R.P.; Hupp, J.T. Metal-organic framework materials as chemical sensors. *Chem. Rev.* **2012**, *112*, 1105–1125. [CrossRef]
35. Yaghi, O.M.; Li, G.; Li, H. Selective binding and removal of guests in a microporous metal–organic framework. *Nature* **1995**, *378*, 703–706. [CrossRef]
36. Li, H.; Eddaoudi, M.; O'Keeffe, M.; Yaghi, O.M. Design and synthesis of an exceptionally stable and highly porous metal organic framework. *Nature* **1999**, *402*, 276–279. [CrossRef]
37. Hu, P.; Morabito, J.V.; Tsung, C.K. Core-shell catalysts of metal nanoparticle core and metal-organic framework shell. *ACS Catal.* **2014**, *4*, 4409–4419. [CrossRef]
38. Vermoortele, F.; Vimont, A.; Serre, C.; De Vos, D. An amino-modified Zr-terephthalate metal–organic framework as an acid–base catalyst for cross-aldol condensation. *Chem. Commun.* **2011**, *47*, 1521–1523. [CrossRef]
39. Huang, Y.B.; Liang, J.; Wang, X.S.; Cao, R. Multifunctional metal-organic framework catalysts: Synergistic catalysis and tandem reactions. *Chem. Soc. Rev.* **2017**, *46*, 126–157.
40. Hinde, C.S.; Webb, W.R.; Chew, B.K.J.; Tan, H.R.; Zhang, W.H.; Hor, T.S.A.; Raja, R. Utilisation of gold nanoparticles on amine-functionalised UiO-66 (NH_2-UiO-66) nanocrystals for selective tandem catalytic reactions. *Chem. Commun.* **2016**, *52*, 6557–6560. [CrossRef]
41. Dhakshinamoorthy, A.; Asiri, A.M.; García, H. Metal-Organic Framework (MOF) Compounds: Photocatalysts for Redox Reactions and Solar Fuel Production. *Angew. Chem. Int. Ed.* **2016**, *55*, 5414–5445.
42. Salunkhe, R.R.; Kaneti, Y.V.; Yamauchi, Y. Metal-Organic Framework-Derived Nanoporous Metal Oxides toward Supercapacitor Applications: Progress and Prospects. *ACS Nano* **2017**, *11*, 5293–5308. [CrossRef] [PubMed]
43. Fang, G.; Wang, Q.; Zhou, J.; Lei, Y.; Chen, Z.; Wang, Z.; Pan, A.; Liang, S. Metal Organic Framework-Templated Synthesis of Bimetallic Selenides with Rich Phase Boundaries for Sodium-Ion Storage and Oxygen Evolution Reaction. *ACS Nano* **2019**, *13*, 5635–5645. [CrossRef] [PubMed]
44. Horcajada, P.; Chalati, T.; Serre, C.; Gillet, B.; Sebrie, C.; Baati, T.; Eubank, J.F.; Heurtaux, D.; Clayette, P.; Kreuz, C.; et al. Porous metal-organic-framework nanoscale carriers as a potential platform for drug deliveryand imaging. *Nat. Mater.* **2010**, *9*, 172–178. [PubMed]

45. Zhuang, J.; Kuo, C.H.; Chou, L.Y.; Liu, D.Y.; Weerapana, E.; Tsung, C.K. Optimized metal-organic-framework nanospheres for drug delivery: Evaluation of small-molecule encapsulation. *ACS Nano* **2014**, *8*, 2812–2819. [PubMed]
46. Ke, F.; Yuan, Y.P.; Qiu, L.G.; Shen, Y.H.; Xie, A.J.; Zhu, J.F.; Tian, X.Y.; Zhang, L.-D. Facile fabrication of magnetic metal-organic framework nanocomposites for potential targeted drug delivery. *J. Mater. Chem.* **2011**, *21*, 3843–3848. [CrossRef]
47. Cai, W.; Chu, C.C.; Liu, G.; Wáng, Y.X.J. Metal-Organic Framework-Based Nanomedicine Platforms for Drug Delivery and Molecular Imaging. *Small* **2015**, *11*, 4806–4822.
48. Wu, M.X.; Yang, Y.W. Metal–Organic Framework (MOF)-Based Drug/Cargo Delivery and Cancer Therapy. *Adv. Mater.* **2017**, *29*, 1–20. [CrossRef]
49. Ma, L.; Wu, C.-D.; Wanderley, M.M.; Lin, W. Single-crystal to single-crystal cross-linking of an interpenetrating chiral metal-organic framework and implications in asymmetric catalysis. *Angew. Chem. Int. Ed.* **2010**, *49*, 8244–8248. [CrossRef]
50. Nguyen, K.D.; Kutzscher, C.; Drache, F.; Senkovska, I.; Kaskel, S. Chiral Functionalization of a Zirconium Metal-Organic Framework (DUT-67) as a Heterogeneous Catalyst in Asymmetric Michael Addition Reaction. *Inorg. Chem.* **2018**, *57*, 1483–1489. [CrossRef]
51. Wang, C.; Zheng, M.; Lin, W. Asymmetric catalysis with chiral porous metal-organic frameworks: Critical issues. *J. Phys. Chem. Lett.* **2011**, *2*, 1701–1709. [CrossRef]
52. Song, F.; Wang, C.; Lin, W. A chiral metal-organic framework for sequential asymmetric catalysis. *Chem. Commun.* **2011**, *47*, 8256–8258. [CrossRef] [PubMed]
53. Tanaka, K.; Oda, S.; Shiro, M. A novel chiral porous metal-organic framework: Asymmetric ring opening reaction of epoxide with amine in the chiral open space. *Chem. Commun.* **2008**, *7*, 820–822. [CrossRef] [PubMed]
54. Wu, C.-D.; Hu, A.; Zhang, L.; Lin, W. A homochiral porous metal-organic framework for highly enantioselective heterogeneous asymmetric catalysis. *J. Am. Chem. Soc.* **2005**, *127*, 8940–8941. [CrossRef]
55. Ma, L.; Falkowski, J.M.; Abney, C.; Lin, W. A series of isoreticular chiral metal–organic frameworks as a tunable platform for asymmetric catalysis. *Nat. Chem.* **2010**, *2*, 838–846. [CrossRef]
56. Surblé, S.; Millange, F.; Serre, C.; Düren, T.; Latroche, M.; Bourrelly, S.; Llewellyn, P.L.; Férey, G. Synthesis of MIL-102, a chromium carboxylate metal-organic framework, with gas sorption analysis. *J. Am. Chem. Soc.* **2006**, *128*, 14889–14896. [CrossRef]
57. Yoon, J.W.; Seo, Y.K.; Hwang, Y.K.; Chang, J.S.; Leclerc, H.; Wuttke, S.; Bazin, P.; Vimont, A.; Daturi, M.; Bloch, E.; et al. Controlled reducibility of a metal-organic framework with coordinatively unsaturated sites for preferential gas sorption. *Angew. Chem. Int. Ed.* **2010**, *49*, 5949–5952. [CrossRef]
58. Dybtsev, D.N.; Chun, H.; Yoon, S.H.; Kim, D.; Kim, K. Microporous Manganese Formate: A Simple Metal-Organic Porous Material with High Framework Stability and Highly Selective Gas Sorption Properties. *J. Am. Chem. Soc.* **2004**, *126*, 32–33.
59. Kondo, A.; Noguchi, H.; Carlucci, L.; Proserpio, D.M.; Ciani, G.; Kajiro, H.; Ohba, T.; Kanoh, H.; Kaneko, K. Double-step gas sorption of a two-dimensional metal-organic framework. *J. Am. Chem. Soc.* **2007**, *129*, 12362–12363. [CrossRef]
60. Li, D.; Yu, S.H.; Jiang, H.L. From UV to Near-Infrared Light-Responsive Metal–Organic Framework Composites: Plasmon and Upconversion Enhanced Photocatalysis. *Adv. Mater.* **2018**, *30*, 1–7. [CrossRef]
61. Fateeva, A.; Chater, P.A.; Ireland, C.P.; Tahir, A.A.; Khimyak, Y.Z.; Wiper, P.V.; Darwent, J.R.; Rosseinsky, M.J. A water-stable porphyrin-based metal-organic framework active for visible-light photocatalysis. *Angew. Chem. Int. Ed.* **2012**, *51*, 7440–7444. [CrossRef] [PubMed]
62. Chen, X.; Kuwahara, Y.; Mori, K.; Louis, C.; Yamashita, H. A hydrophobic titanium doped zirconium-based metal organic framework for photocatalytic hydrogen peroxide production in a two-phase system. *J. Mater. Chem. A* **2020**, *8*, 1904–1910.
63. Chen, X.; Kondo, Y.; Kuwahara, Y.; Mori, K.; Louis, C.; Yamashita, H. Metal-organic framework-based nanomaterials for photocatalytic hydrogen peroxide production. *Phys. Chem. Chem. Phys.* **2020**, *22*, 14404–14414. [CrossRef] [PubMed]
64. Wu, X.P.; Gagliardi, L.; Truhlar, D.G. Cerium Metal-Organic Framework for Photocatalysis. *J. Am. Chem. Soc.* **2018**, *140*, 7904–7912. [CrossRef] [PubMed]
65. Zhou, H.C.; Long, J.R.; Yaghi, O.M. Introduction to metal-organic frameworks. *Chem. Rev.* **2012**, *112*, 673–674. [CrossRef] [PubMed]

66. Alvaro, M.; Carbonell, E.; Ferrer, B.; Llabrés I Xamena, F.X.; Garcia, H. Semiconductor behavior of a metal-organic framework (MOF). *Chem. Eur. J.* **2007**, *13*, 5106–5112. [CrossRef] [PubMed]
67. Bordiga, S.; Lamberti, C.; Ricchiardi, G.; Regli, L.; Bonino, F.; Damin, A.; Lillerud, K.P.; Bjorgen, M.; Zecchina, A. Electronic and vibrational properties of a MOF-5 metal-organic framework: ZnO quantum dot behaviour. *Chem. Commun.* **2004**, *5*, 2300–2301. [CrossRef]
68. Subudhi, S.; Rath, D.; Parida, K.M. A mechanistic approach towards the photocatalytic organic transformations over functionalised metal organic frameworks: A review. *Catal. Sci. Technol.* **2018**, *8*, 679–696.
69. Beyzavi, M.H.; Stephenson, C.J.; Liu, Y.; Karagiaridi, O.; Hupp, J.T.; Farha, O.K. Metal–Organic Framework-Based Catalysts: Chemical Fixation of CO_2 with Epoxides Leading to Cyclic Organic Carbonates. *Front. Energy Res.* **2015**, *2*, 63. [CrossRef]
70. He, H.; Perman, J.A.; Zhu, G.; Ma, S. Metal-Organic Frameworks for CO_2 Chemical Transformations. *Small* **2016**, *12*, 6309–6324. [CrossRef]
71. Luciani, G.; Imparato, C.; Vitiello, G. Photosensitive hybrid nanostructured materials: The big challenges for sunlight capture. *Catalysts* **2020**, *10*, 103. [CrossRef]
72. Liu, C.; Wang, W.; Liu, B.; Qiao, J.; Lv, L.; Gao, X.; Zhang, X.; Xu, D.; Liu, W.; Liu, J.; et al. Recent Advances in MOF-based Nanocatalysts for Photo-Promoted CO_2 Reduction Applications. *Catalysts* **2019**, *9*, 658. [CrossRef]
73. Alkhatib, I.I.; Garlisi, C.; Pagliaro, M.; Al-Ali, K.; Palmisano, G. Metal-organic frameworks for photocatalytic CO_2 reduction under visible radiation: A review of strategies and applications. *Catal. Today* **2020**, *340*, 209–224. [CrossRef]
74. Wang, J.L.; Wang, C.; Lin, W. Metal-organic frameworks for light harvesting and photocatalysis. *ACS Catal.* **2012**, *2*, 2630–2640. [CrossRef]
75. Zhang, L.; Zhang, J. Metal-organic frameworks for CO_2 photoreduction. *Front. Energy* **2019**, *13*, 221–250.
76. Kidanemariam, A.; Lee, J.; Park, J. Recent innovation of metal-organic frameworks for carbon dioxide photocatalytic reduction. *Polymers* **2019**, *11*, 2090. [CrossRef]
77. Rasheed, T.; Rizwan, K.; Bilal, M.; Iqbal, H.M.N. Metal-Organic Framework-Based Engineered Materials—Fundamentals and Applications. *Molecules* **2020**, *25*, 1598. [CrossRef]
78. Crake, A. Metal-organic frameworks based materials for photocatalytic CO_2 reduction. *Mater. Sci. Technol.* **2017**, *33*, 1737–1749. [CrossRef]
79. Huang, C.W.; Nguyen, V.H.; Zhou, S.R.; Hsu, S.Y.; Tan, J.X.; Wu, K.C.W. Metal-organic frameworks: Preparation and applications in highly efficient heterogeneous photocatalysis. *Sustain. Energy Fuels* **2020**, *4*, 504–521.
80. Zhang, H.; Wei, J.; Dong, J.; Liu, G.; Shi, L.; An, P.; Zhao, G.; Kong, J.; Wang, X.; Meng, X.; et al. Efficient Visible-Light-Driven Carbon Dioxide Reduction by a Single-Atom Implanted Metal–Organic Framework. *Angew. Chem. Int. Ed.* **2016**, *55*, 14310–14314. [CrossRef]
81. Li, D.; Kassymova, M.; Cai, X.; Zang, S.Q.; Jiang, H.L. Photocatalytic CO_2 reduction over metal-organic framework-based materials. *Coord. Chem. Rev.* **2020**, *412*, 213262. [CrossRef]
82. Zhang, T.; Lin, W. Metal-organic frameworks for artificial photosynthesis and photocatalysis. *Chem. Soc. Rev.* **2014**, *43*, 5982–5993. [CrossRef] [PubMed]
83. Verma, P.; Kuwahara, Y.; Mori, K.; Yamashita, H. Design of silver-based controlled nanostructures for plasmonic catalysis under visible light irradiation. *Bull. Chem. Soc. Jpn.* **2019**, *92*, 19–29. [CrossRef]
84. Yamashita, H.; Mori, K.; Kuwahara, Y.; Kamegawa, T.; Wen, M.; Verma, P.; Che, M. Single-site and nano-confined photocatalysts designed in porous materials for environmental uses and solar fuels. *Chem. Soc. Rev.* **2018**, *47*, 8072–8096. [PubMed]
85. Verma, P.; Yuan, K.; Kuwahara, Y.; Mori, K.; Yamashita, H. Enhancement of plasmonic activity by Pt/Ag bimetallic nanocatalyst supported on mesoporous silica in the hydrogen production from hydrogen storage material. *Appl. Catal. B Environ.* **2018**, *223*, 10–15. [CrossRef]
86. Verma, P.; Kuwahara, Y.; Mori, K.; Yamashita, H. Enhancement of Ag-based plasmonic photocatalysis in hydrogen production from ammonia borane by the assistance of single-site Ti-oxide moieties within a silica framework. *Chem. Eur. J.* **2017**, *23*, 3616–3622. [CrossRef] [PubMed]
87. Verma, P.; Kuwahara, Y.; Mori, K.; Yamashita, H. Synthesis and characterization of a Pd/Ag bimetallic nanocatalyst on SBA-15 mesoporous silica as a plasmonic catalyst. *J. Mater. Chem. A* **2015**, *3*, 18889–18897. [CrossRef]

88. Verma, P.; Mori, K.; Kuwahara, Y.; Cho, S.J.; Yamashita, H. Synthesis of plasmonic gold nanoparticles supported on morphology-controlled TiO_2 for aerobic alcohol oxidation. *Catal. Today* **2020**, *352*, 255–261. [CrossRef]
89. Verma, P.; Kuwahara, Y.; Mori, K.; Raja, R.; Yamashita, H. Functionalized mesoporous SBA-15 silica: Recent trends and catalytic applications. *Nanoscale* **2020**, *12*, 11333–11363.
90. Langhammer, C.; Yuan, Z.; Zorić, I.; Kasemo, B. Plasmonic properties of supported Pt and Pd nanostructures. *Nano Lett.* **2006**, *6*, 833–838. [CrossRef]
91. Jo, S.; Verma, P.; Kuwahara, Y.; Mori, K.; Choi, W.; Yamashita, H. Enhanced hydrogen production from ammonia borane using controlled plasmonic performance of Au nanoparticles deposited on TiO_2. *J. Mater. Chem. A* **2017**, *5*, 21883–21892. [CrossRef]
92. Verma, P.; Kuwahara, Y.; Mori, K.; Yamashita, H. Synthesis of mesoporous silica-supported Ag nanorod-based bimetallic catalysts and investigation of their plasmonic activity under visible light irradiation. *Catal. Sci. Technol.* **2017**, *7*, 2551–2558. [CrossRef]
93. Verma, P.; Navlani-garcía, M.; Kuwahara, Y.; Mori, K.; Yamashita, H. Mesoporous silica supported Pd/Ag bimetallic nanoparticles as a plasmonic catalyst for chemoselective hydrogenation of p-nitrostyrene under visible light irradiation. *J. Chem. Sci.* **2017**, *129*, 1661–1669. [CrossRef]
94. Mori, K.; Verma, P.; Hayashi, R.; Fuku, K.; Yamashita, H. Color-Controlled Ag Nanoparticles and Nanorods within Confined Mesopores: Microwave-Assisted Rapid Synthesis and Application in Plasmonic Catalysis under Visible-Light Irradiation. *Chem. Eur. J.* **2015**, *21*, 11885–11893. [CrossRef]
95. Verma, P.; Kuwahara, Y.; Mori, K.; Yamashita, H. Pd/Ag and Pd/Au bimetallic nanocatalysts on mesoporous silica for plasmon-mediated enhanced catalytic activity under visible light irradiation. *J. Mater. Chem. A* **2016**, *4*, 10142–10150.
96. Chen, M.; Han, L.; Zhou, J.; Sun, C.; Hu, C.; Wang, X.; Su, Z. Photoreduction of carbon dioxide under visible light by ultra-small Ag nanoparticles doped into Co-ZIF-9. *Nanotechnology* **2018**, *29*, 284003. [CrossRef]
97. Guo, F.; Yang, S.; Liu, Y.; Wang, P.; Huang, J.; Sun, W.Y. Size Engineering of Metal-Organic Framework MIL-101(Cr)-Ag Hybrids for Photocatalytic CO_2 Reduction. *ACS Catal.* **2019**, *9*, 8464–8470.
98. Deng, X.; Yang, L.; Huang, H.; Yang, Y.; Feng, S.; Zeng, M.; Li, Q.; Xu, D. Shape-Defined Hollow Structural Co-MOF-74 and Metal Nanoparticles@Co-MOF-74 Composite through a Transformation Strategy for Enhanced Photocatalysis Performance. *Small* **2019**, *15*, 1–7. [CrossRef]
99. Chen, L.; Wang, Y.; Yu, F.; Shen, X.; Duan, C. A simple strategy for engineering heterostructures of Au nanoparticle-loaded metal-organic framework nanosheets to achieve plasmon-enhanced photocatalytic CO_2 conversion under visible light. *J. Mater. Chem. A* **2019**, *7*, 11355–11361. [CrossRef]
100. Khaletskaya, K.; Pougin, A.; Medishetty, R.; Rösler, C.; Wiktor, C.; Strunk, J.; Fischer, R.A. Fabrication of Gold/Titania Photocatalyst for CO_2 Reduction Based on Pyrolytic Conversion of the Metal-Organic Framework NH_2-MIL-125(Ti) Loaded with Gold Nanoparticles. *Chem. Mater.* **2015**, *27*, 7248–7257.
101. Sun, D.; Liu, W.; Fu, Y.; Fang, Z.; Sun, F.; Fu, X.; Zhang, Y.; Li, Z. Noble metals can have different effects on photocatalysis over metal-organic frameworks (MOFs): A case study on M/NH_2-MIL-125(Ti) (M=Pt and Au). *Chem. Eur. J.* **2014**, *20*, 4780–4788. [CrossRef] [PubMed]
102. Guo, F.; Wei, Y.P.; Wang, S.Q.; Zhang, X.Y.; Wang, F.M.; Sun, W.Y. Pt nanoparticles embedded in flowerlike NH_2-UiO-68 for enhanced photocatalytic carbon dioxide reduction. *J. Mater. Chem. A* **2019**, *7*, 26490–26495. [CrossRef]
103. Chambers, M.B.; Wang, X.; Elgrishi, N.; Hendon, C.H.; Walsh, A.; Bonnefoy, J.; Canivet, J.; Quadrelli, E.A.; Farrusseng, D.; Mellot-Draznieks, C.; et al. Photocatalytic Carbon Dioxide Reduction with Rhodium-based Catalysts in Solution and Heterogenized within Metal-Organic Frameworks. *ChemSusChem* **2015**, *8*, 603–608. [CrossRef] [PubMed]
104. Wang, S.; Yao, W.; Lin, J.; Ding, Z.; Wang, X. Cobalt Imidazolate Metal-Organic Frameworks Photosplit CO_2 under Mild Reaction Conditions. *Angew. Chem.* **2014**, *53*, 1034–1038.
105. Wang, S.; Wang, X. Photocatalytic CO_2 reduction by CdS promoted with a zeolitic imidazolate framework. *Appl. Catal. B Environ.* **2015**, *162*, 494–500.
106. Mei, B.; Pougin, A.; Strunk, J. Influence of photodeposited gold nanoparticles on the photocatalytic activity of titanate species in the reduction of CO_2 to hydrocarbons. *J. Catal.* **2013**, *306*, 184–189. [CrossRef]
107. Dan-Hardi, M.; Serre, C.; Frot, T.; Rozes, L.; Maurin, G.; Sanchez, C.; Férey, G. A new photoactive crystalline highly porous titanium(IV) dicarboxylate. *J. Am. Chem. Soc.* **2009**, *131*, 10857–10859. [CrossRef] [PubMed]

108. Fu, Y.; Sun, D.; Chen, Y.; Huang, R.; Ding, Z.; Fu, X.; Li, Z. An amine-functionalized titanium metal-organic framework photocatalyst with visible-light-induced activity for CO_2 reduction. *Angew. Chem. Int. Ed.* **2012**, *51*, 3364–3367.
109. Sun, D.; Li, Z. Robust Ti- and Zr-Based Metal-Organic Frameworks for Photocatalysis. *Chin. J. Chem.* **2017**, *35*, 135–147. [CrossRef]
110. Horiuchi, Y.; Toyao, T.; Saito, M.; Mochizuki, K.; Iwata, M.; Higashimura, H.; Anpo, M.; Matsuoka, M. Visible-light-promoted photocatalytic hydrogen production by using an amino-functionalized Ti(IV) metal-organic framework. *J. Phys. Chem. C* **2012**, *116*, 20848–20853.
111. Deria, P.; Mondloch, J.E.; Karagiaridi, O.; Bury, W.; Hupp, J.T.; Farha, O.K. Beyond post-synthesis modification: Evolution of metal-organic frameworks via building block replacement. *Chem. Soc. Rev.* **2014**, *43*, 5896–5912. [PubMed]
112. Han, B.; Ou, X.; Deng, Z.; Song, Y.; Tian, C.; Deng, H.; Xu, Y.J.; Lin, Z. Nickel Metal–Organic Framework Monolayers for Photoreduction of Diluted CO_2: Metal-Node-Dependent Activity and Selectivity. *Angew. Chem. Int. Ed.* **2018**, *57*, 16811–16815.
113. Jiang, H.; Gong, S.; Xu, S.; Shi, P.; Fan, J.; Cecen, V.; Xu, Q.; Min, Y. Bimetal composites for photocatalytic reduction of CO_2 to CO in the near-infrared region by the SPR effect. *Dalt. Trans.* **2020**, *49*, 5074–5086. [CrossRef] [PubMed]
114. Kong, Z.C.; Liao, J.F.; Dong, Y.J.; Xu, Y.F.; Chen, H.Y.; Kuang, D.-B.; Su, C.Y. Core@shell $CsPbBr_3$@zeolitic imidazolate framework nanocomposite for efficient photocatalytic CO_2 reduction. *ACS Energy Lett.* **2018**, *3*, 2656–2662. [CrossRef]
115. Xu, J.; Liu, X.; Zhou, Z.; Xu, M. Photocatalytic CO_2 reduction catalyzed by metalloporphyrin: Understanding of cobalt and nickel sites in activity and adsorption. *Appl. Surf. Sci.* **2020**, *513*, 145801. [CrossRef]
116. Xu, Y.F.; Yang, M.Z.; Chen, B.X.; Wang, X.D.; Chen, H.Y.; Kuang, D.-B.; Su, C.Y. A $CsPbBr_3$ Perovskite Quantum Dot/Graphene Oxide Composite for Photocatalytic CO_2 Reduction. *J. Am. Chem. Soc.* **2017**, *139*, 5660–5663. [CrossRef]
117. Zhao, L.; Zhao, Z.; Li, Y.; Chu, X.; Li, Z.; Qu, Y.; Bai, L.; Jing, L. The synthesis of interface-modulated ultrathin Ni(ii) MOF/g-C_3N_4 heterojunctions as efficient photocatalysts for CO_2 reduction. *Nanoscale* **2020**, *12*, 10010–10018. [CrossRef]
118. Wang, D.; Huang, R.; Liu, W.; Sun, D.; Li, Z. Fe-based MOFs for photocatalytic CO_2 reduction: Role of coordination unsaturated sites and dual excitation pathways. *ACS Catal.* **2014**, *4*, 4254–4260. [CrossRef]
119. Dao, X.Y.; Guo, J.H.; Wei, Y.P.; Guo, F.; Liu, Y.; Sun, W.Y. Solvent-free photoreduction of CO_2 to CO catalyzed by Fe-MOFs with superior selectivity. *Inorg. Chem.* **2019**, *58*, 8517–8524. [CrossRef]
120. Wang, S.S.; Huang, H.H.; Liu, M.; Yao, S.; Guo, S.; Wang, J.W.; Zhang, Z.M.; Lu, T.B. Encapsulation of Single Iron Sites in a Metal-Porphyrin Framework for High-Performance Photocatalytic CO_2 Reduction. *Inorg. Chem.* **2020**, *59*, 6301–6307. [CrossRef]
121. Wu, L.Y.; Mu, Y.F.; Guo, X.X.; Zhang, W.; Zhang, Z.M.; Zhang, M.; Lu, T.B. Encapsulating Perovskite Quantum Dots in Iron-Based Metal–Organic Frameworks (MOFs) for Efficient Photocatalytic CO_2 Reduction. *Angew. Chem. Int. Ed.* **2019**, *58*, 9491–9495. [CrossRef] [PubMed]
122. Sun, D.; Fu, Y.; Liu, W.; Ye, L.; Wang, D.; Yang, L.; Fu, X.; Li, Z. Studies on photocatalytic CO_2 reduction over NH 2-uio-66(Zr) and its derivatives: Towards a better understanding of photocatalysis on metal-organic frameworks. *Chem. Eur. J.* **2013**, *19*, 14279–14285. [CrossRef] [PubMed]
123. Mu, Q.; Zhu, W.; Li, X.; Zhang, C.; Su, Y.; Lian, Y.; Qi, P.; Deng, Z.; Zhang, D.; Wang, S.; et al. Electrostatic charge transfer for boosting the photocatalytic CO_2 reduction on metal centers of 2D MOF/rGO heterostructure. *Appl. Catal. B Environ.* **2020**, *262*, 118144. [CrossRef]
124. Li, S.; Ji, K.; Zhang, M.; He, C.; Wang, J.; Li, Z. Boosting the photocatalytic CO_2 reduction of metal-organic frameworks by encapsulating carbon dots. *Nanoscale* **2020**, *12*, 9533–9540.
125. Liu, S.; Chen, F.; Li, S.; Peng, X.; Xiong, Y. Enhanced photocatalytic conversion of greenhouse gas CO_2 into solar fuels over g-C_3N_4 nanotubes with decorated transparent ZIF-8 nanoclusters. *Appl. Catal. B Environ.* **2017**, *211*, 1–10. [CrossRef]
126. Wang, M.; Liu, J.; Guo, C.; Gao, X.; Gong, C.; Wang, Y.; Liu, B.; Li, X.; Gurzadyan, G.G.; Sun, L. Metal-organic frameworks (ZIF-67) as efficient cocatalysts for photocatalytic reduction of CO_2: The role of the morphology effect. *J. Mater. Chem. A* **2018**, *6*, 4768–4775. [CrossRef]

127. Ren, J.T.; Zheng, Y.L.; Yuan, K.; Zhou, L.; Wu, K.; Zhang, Y.W. Self-templated synthesis of Co_3O_4 hierarchical nanosheets from a metal-organic framework for efficient visible-light photocatalytic CO_2 reduction. *Nanoscale* **2020**, *12*, 755–762. [CrossRef]
128. Chen, S.; Yu, J.; Zhang, J. Enhanced photocatalytic CO_2 reduction activity of MOF-derived ZnO/NiO porous hollow spheres. *J. CO2 Util.* **2018**, *24*, 548–554. [CrossRef]
129. Wang, C.; Xie, Z.; Dekrafft, K.E.; Lin, W. Doping metal-organic frameworks for water oxidation, carbon dioxide reduction, and organic photocatalysis. *J. Am. Chem. Soc.* **2011**, *133*, 13445–13454. [CrossRef]
130. Benseghir, Y.; Lemarchand, A.; Duguet, M.; Mialane, P.; Gomez-Mingot, M.; Roch-Marchal, C.; Pino, T.; Ha-Thi, M.H.; Haouas, M.; Fontecave, M.; et al. Co-immobilization of a Rh Catalyst and a Keggin Polyoxometalate in the UiO-67 Zr-Based Metal-Organic Framework: In Depth Structural Characterization and Photocatalytic Properties for CO_2 Reduction. *J. Am. Chem. Soc.* **2020**, *142*, 9428–9438. [CrossRef]
131. Gao, X.; Guo, B.; Guo, C.; Meng, Q.; Liang, J.; Liu, J. Zirconium-Based Metal-Organic Framework for Efficient Photocatalytic Reduction of CO_2 to CO: The Influence of Doped Metal Ions. *ACS Appl. Mater. Interfaces* **2020**, *12*, 24059–24065. [CrossRef] [PubMed]